Argonne National Laboratory

PERFORMANCE CHARACTERISTICS OF A LIQUID METAL MHD GENERATOR

by

Michael Petrick and Kung-You Lee

ARGONNE NATIONAL LABORATORY
9700 South Cass Avenue
Argonne, Illinois 60440

PERFORMANCE CHARACTERISTICS OF
A LIQUID METAL MHD GENERATOR

by

Michael Petrick and Kung-You Lee

Reactor Engineering Division

July 1964

TABLE OF CONTENTS

TABLE OF CONTENTS

5

LIST OF FIGURES

No.	Title	Page
1.	Liquid Metal MHD Cycle	11
2.	Schematic Diagram of Magnetohydrodynamic Channel	13
3.	Schematic Diagram of Velocity Distribution	14
4.	Electrical Circuit of Experimental MHD Generator and Load	23
5.	Schematic Diagram of Experimental Loop	25
6.	Schematic Diagram of NaK Pump	25
7.	Schematic Diagram of MHD Generator Section	28
8.	MHD Generator Section, Electromagnet, and Photomultiplier Tube Assembly	28
9.	System for Measuring Pressure Drop in Test Section	29
10.	Comparison of Calculated and Measured Voltage; Test Series I: B_o=8800, 6400, and 4350 Gauss	33
11.	Comparison of Calculated and Measured Voltage; Test Series I: B_o=8450 Gauss	33
12.	Comparison of Calculated and Measured Voltage; Test Series I: B_o=7940 Gauss	33
13.	Comparison of Calculated and Measured Voltage; Test Series I: B_o=7320 Gauss	33
14.	Comparison of Calculated and Measured Pressure Drop; Test Series I: B_o=8800 and 6400 Gauss	35
15.	Comparison of Calculated and Measured Pressure Drop; Test Series I: B_o=8450 and 4350 Gauss	35
16.	Comparison of Calculated and Measured Pressure Drop; Test Series I: B_o=7940 Gauss	35
17.	Comparison of Calculated and Measured Pressure Drop; Test Series I: B_o=7320 Gauss	35
18.	Comparison of Calculated and Measured Voltage; Test Series II: B_o=8900, 6500, and 4350 Gauss	36
19.	Comparison of Calculated and Measured Voltage; Test Series II: B_o=8500 Gauss	36
20.	Comparison of Calculated and Measured Voltage; Test Series II: B_o=8000 Gauss	37

LIST OF FIGURES

LIST OF FIGURES

LIST OF TABLES

PERFORMANCE CHARACTERISTICS OF
A LIQUID METAL MHD GENERATOR

by

Michael Petrick and Kung-You Lee

ABSTRACT

An experimental study was made of the performance characteristics of a liquid metal MHD generator utilizing single-phase NaK and two-phase NaK-N_2 fluids. The purpose of this study was to compare the generator performance with theory for single-phase flow and to determine the effects of the introduction of the gaseous phase on the generator output and efficiency. Data were taken over the following parameter ranges: fluid velocity, 1.11 to 10.94 ft/sec; mixture quality, 0 to 0.0156; volumetric void fraction, 0 to 0.66. The variation of the Hartmann number and the magnetic Reynolds number (based on the height of the channel) corresponding to these parameter ranges was 88 to 178, and 0.035 to 0.35, respectively.

An extension was made of Hartmann's flow analysis to a generator duct that takes into account end losses and power dissipation in the duct wall. The agreement between the theory and the data was good. The end loss correction factors used were those proposed by Sutton. Comparison of the data with the theory tended to validate the use of these factors. The open-circuit and closed-circuit voltage, current, and power output could be computed accurately, but the measured pressure drop deviated substantially from the predicted values.

From the NaK-N_2 two-phase flow tests, an empirical relationship was developed for the two-phase conductivity as a function of the void volume fraction. The relationship is

$$\sigma_{TP}/\sigma = \exp(-3.8\alpha).$$

The implications of two-phase conductivity on MHD generator performance are discussed.

8

NOMENCLATURE

Symbol	Definition
A	Cross-sectional area of channel = $4ba$
a	Half-width of the generator channel in x direction
$\underset{\sim}{B}$	Magnetic field
B_o	Applied magnetic field in y direction
$B_{x,y,z}$	Induced magnetic field in x, y, and z directions
b	Half-height of the generator channel in y direction
c	Channel aspect ratio = $L/2a$
$C_1 \ldots C_6$	Integration constants
$\underset{\sim}{E}$	Electric field
E_i	Induced emf
E_x	Electric field in x direction
g	Gravitational force
Ha	Hartmann number = $bB_o(\sigma/\mu)^{1/2}$
$i_{x,y,z}$	Unit vector in x, y, and z directions
I	Total current
I_2	Current in external circuit
I_w	Current in the conducting walls
j	Current density
L	Length of the generator channel in z direction; length of the electrode; or length of applied magnetic field
M	Mass flow rate
p	Pressure
P_g	Generator power
P_o	Output power
P_p	Input power or flow work
P_α	Power output as function of α
R_c	Contact resistance between fluid and electrode
R_e	End-loss resistance
R_i	Internal resistance of the MHD generator = $a/bL\sigma$
R_o	Load resistance

Symbol	Definition
R_w	Channel wall resistance
R_{BB}	Bus-bar resistance
R_{sh}	Shunt resistance
R_{ss}	Fixed resistance as a part of load
R_o'	$R_{sh} + R_{ss} + R_{BB}$
t	Time
$\underset{\sim}{U}$	Velocity
U_m	Mean velocity of liquid metal
V	Voltage between two electrodes with $R_c = 0$
V_1	Voltage between measuring points 1-1'
V_2	Voltage between measuring points 2-2'
V_{cc}	Open-circuit voltage
w	Velocity component in z direction
x,y,z	Coordinates

Greek

Symbol	Definition
α	Void fraction
γ	R_o/R_i
Δ	Difference between two quantities
ϵ	Generator efficiency
η	Loading factor, excluding end-loss correction = $1+\gamma)$
η'	Loading factor, including end-loss correction
η''	Loading factor, including end-loss correction and exponential field decay
μ	Absolute viscosity
μ_e	Permeability
ρ	Mass density
σ	Electrical conductivity

Subscript

Symbol	Definition
TP	Two-phase

I. INTRODUCTION

The interaction of a moving conductor with a magnetic field is the classical method of electric power generation. The conductor can be a metallic solid such as used in conventional rotating systems, or it can be a fluid. In 1831, Faraday attempted to demonstrate magnetohydrodynamic (MHD) power generation by measuring a potential developed from the interaction of the tidal currents in the River Thames with the terrestrial magnetic field. Although unsuccessful, he set forth the basic principles of the interaction between magnetic fields and flowing, electrically-conducting fluids which are applicable to MHD power generation.

The effort on MHD power generation has increased sharply in the past few years, as evidenced by the wealth of open literature on the subject. Several excellent status reports and surveys have been published recently.[1,2] The principal effort has been on compressible MHD channel flow with ionized gases. From these studies, it has become evident that serious technological problems exist in the plasma MHD cycle, notably the attainment of adequate electrical conductivity of the plasma within the temperature limits imposed by materials considerations.

The alternative to the low-conductivity plasma is the use of a liquid metal as the working fluid. The electrical conductivity of a liquid metal is at least four orders of magnitude greater than that of an ionized gas. On the other hand, the fluid velocities that can be obtained in a liquid metal generator are between one and two orders of magnitude less than velocities that can be achieved in a plasma system. However, since the power density of a generator is proportional to the product σU_m^2, the power density of the liquid metal MHD generator appears to be at least equal to that of the plasma system, and may be substantially greater. A major consideration is that this equivalence is achieved in the liquid metal system at a temperature that is within the scope of current materials technology.

Since it has no rotating parts, the liquid metal MHD system appears to be especially adaptable as a sustained power source for space application. Typical power cycles proposed for this purpose are those due to Elliott[3] and Brown et al.[4]

Elliott's proposed cycle (shown in Fig. 1) consists of two loops and two immiscible liquid metals as working fluids. In the vapor loop, the fluid is pumped into the mixer where it is vaporized upon contact with the higher-temperature fluid emerging from the liquid loop. The vapor expands with the liquid through a two-phase nozzle, is separated from the liquid in a separator, is condensed in a radiator condenser, and then is pumped back into the mixer. In the liquid loop, the liquid is heated in the reactor, passes into the mixer where it gives up heat during vaporization of the condensate, is accelerated

by the vapor in the nozzle, passes through the separator into the MHD generator where the production of electric power takes place, and then is returned to the reactor by means of a diffuser.
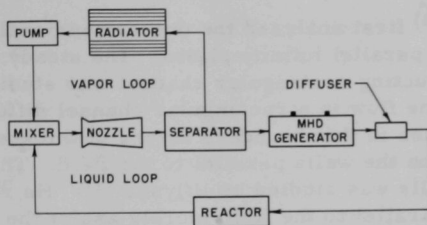
Fig. 1. Liquid Metal MHD Cycle

The key to this cycle is the performance characteristics of the nozzle, the separator, and the MHD generator. Considerable information has been accumulated on the efficiency of the expansion of two-phase mixtures through nozzles. Based on isentropic homogeneous expansion, the data indicate that nozzles may be designed to yield efficiencies as high as 70-80%. However, the pressure-drop losses through the separator are large, and the completeness of separation between the phases that can be achieved in a practical system is uncertain.

The effect of the vapor phase on generator performance is unknown and not readily predictable since the conductivity data on two-phase mixtures are not available. The major analytical effort has been on MHD generators operating under highly idealized conditions.

Because of the importance of the MHD generator in regard to overall cycle efficiency, an experimental study of the generator was undertaken. Little information or data are available on the performance characteristics of a liquid metal MHD generator. The primary objectives of this study were: (1) to compare generator performance data with theory for single-phase flow; and (2) to determine the efficiency and performance of an MHD generator utilizing two-phase mixtures.

II. THEORETICAL ANALYSIS

A. The Ideal Generator Based on Hartmann Flow*

Hartmann[8] first analyzed the one-dimensional flow of a conducting liquid between two parallel infinite plates. The steady flow of conducting fluids in a nonconducting rectangular channel was studied by Shercliff.[9] He observed that the flow in a rectangular channel differed from that between parallel planes in that boundary layers of thickness proportional to $(Ha)^{-1/2}$ occurred on the walls parallel to the field. The case of ideally-conducting side walls was studied by Uflyand.[10] He reported that end-conducting walls parallel to the field merely assist the exchange of current between the core of uniform flow and the side boundary layers and walls. In all cases, the solution was represented by a trigonometric series obtained by the method of particular solutions. Williams[11] developed the asymptotic forms. Ryabinin and Khozhainov[12] approximated the problem by neglecting the induced field. The approximate solution was found to be reasonably accurate when compared with experimental results. Furthermore, in the laminar flow region of a channel whose width is much larger than its height, the results were very close to those of Hartmann. Therefore, it is reasonable to assume that for a channel with a >> b, the flow will be essentially one-dimensional. Further assumptions are

(1) The flow is steady, incompressible, and in the z direction only.

(2) The velocity component w is a function of y only.

(3) The length of the channel (L) is much larger than its width (2a) and height (2b); i.e., L >> 2a >> 2b.

(4) The applied magnetic field (B_O) is uniform time-invariant and in the y direction only. There is no applied electric field.

(5) The fluid is electrically neutral, with a constant scalar conductivity.

Consider a rectangular channel as shown in Fig. 2. Let the applied magnetic field B_O be uniform and in the y direction only, with the liquid moving in the z direction. Under these assumptions, and when electrical displacement currents are neglected, the governing electromagnetic equations are, in the MKS system of units

$$\nabla \cdot \underset{\sim}{E} = 0; \tag{1a}$$

---

*The flow analysis discussed in this section was performed by Dr. Liu, Associate Professor of Northwestern University. Subsequently, it was brought to the attention of the authors that essentially similar results were derived recently by other workers[5-7] and were available in report or note form.

$$\nabla \times \underset{\sim}{E} = 0; \tag{1b}$$

$$\nabla \cdot \underset{\sim}{B} = 0; \tag{1c}$$

$$\frac{1}{\mu_e} \nabla \times \underset{\sim}{B} = \underset{\sim}{j}. \tag{1d}$$
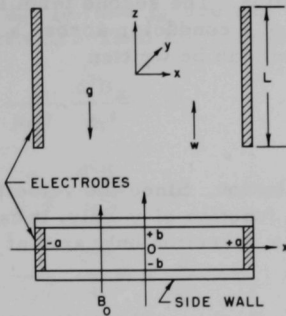
Fig. 2

Schematic Diagram of Magneto-hydrodynamic Channel

If the Hall effect is neglected, Ohm's law for a moving medium can be written as

$$\underset{\sim}{j} = \sigma(\underset{\sim}{E} + \underset{\sim}{U} \times \underset{\sim}{B}). \tag{2}$$

The hydrodynamic equations to be satisfied are as follows:

Equation of Continuity

$$\nabla \cdot \underset{\sim}{U} = 0. \tag{3}$$

Momentum Equation

$$\rho \frac{d\underset{\sim}{U}}{dt} = -\nabla p + \underset{\sim}{j} \times \underset{\sim}{B} + \mu \nabla^2 \underset{\sim}{U} + \rho \underset{\sim}{g}, \tag{4}$$

where

$$\frac{d}{dt} = \frac{\partial}{\partial t} + \underset{\sim}{U} \cdot \nabla$$

is the substantial derivative.

Equations (1) and (2) can be combined to yield the induction equation

$$\frac{1}{\mu_e \sigma} \nabla^2 \underline{B} + \nabla \times (\underline{U} \times \underline{B}) = 0, \tag{5}$$

which describes the variation of the magnetic field. Thus Eqs. (3), (4), and (5) are the set of governing equations that have to be solved for the specified boundary conditions.

In Ohm's law, the first term on the right-hand side of Eq. (2) is the electric field due to the charge distribution. The second term is the induced emf field that is due to the motion of a conductor across a magnetic field. The equation for the induced emf can be written

$$E_i = \int \underline{U} \times \underline{B} \cdot d\underline{s},$$

for which E_i depends on the velocity distribution. Since the velocity component w is in the z direction and is a function of y only, it can be assumed that the electric field E is in the x direction only and, at most, may depend on y.

The viscosity of the fluid retards the flow near the wall. With no magnetic field, the velocity will have a parabolic distribution as shown schematically in Fig. 3. The effect of the magnetic field is to give rise to a magnetic force $\underline{j} \times \underline{B}$, which is equivalent to a tension $B^2/2$ along the lines of force together with an equal pressure transverse to them. (This is the form usually quoted for the Maxwell stresses.) Therefore, the field produces an additional pressure on fluid motion perpendicular to the lines of force, and the velocity distribution is flattened when a conducting fluid moves in a transverse field.
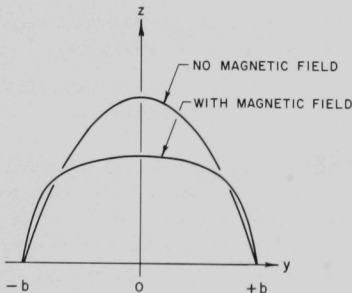
Fig. 3

Schematic Diagram of
Velocity Distribution

Since the induced emf depends on the velocity distribution, it will also decrease near the walls and will have a distribution similar to that of the velocity. Due to the induced emf, a current will flow in the x direction which will, in turn, cause an induced magnetic field around it.

Based upon the assumptions stated previously,

$$\underset{\sim}{B} = \underset{\sim}{i}_x B_x(y) + \underset{\sim}{i}_y B_y(y) + \underset{\sim}{i}_z B_z(y),$$

and

$$\underset{\sim}{U} = \underset{\sim}{i}_z w(y),$$

where $\underset{\sim}{i}_x$, $\underset{\sim}{i}_y$, and $\underset{\sim}{i}_z$ are unit vectors in x, y, and z directions, respectively. Then Eq. (5) has the following components:

$$\frac{1}{\mu_e \sigma} \frac{d^2 B_x}{dy^2} = 0; \tag{6a}$$

$$\frac{1}{\mu_e \sigma} \frac{d^2 B_y}{dy^2} = 0; \tag{6b}$$

$$\frac{1}{\mu_e \sigma} \frac{d^2 B_z}{dy^2} + \frac{d}{dy} (w B_y) = 0. \tag{6c}$$

Integration of Eq. (6a) yields

$$B_x = C_1 y + C_2.$$

The only magnetic field outside the region is the uniformly applied field B_0, which is in the y direction; thus,

$$B_x = 0 \text{ at } y = \pm b.$$

Therefore,

$$B_x = 0.$$

Integration of Eq. (6b) yields

$$B_y = C_3 y + C_4.$$

The boundary condition is

$$B_y = B_0 \text{ at } y = \pm b;$$

therefore,

$$C_3 = 0,$$

and

$$C_4 = B_0.$$

Hence,

$$\underset{\sim}{B} = 0, \ B_o, \ B_z(y).$$

The current density can be calculated from Eq. (1d). The only nonvanishing component is

$$j_x = \frac{1}{\mu_e} \frac{dB_z}{dy}. \tag{7}$$

The electric field intensity E is given by Ohm's law. Again, the only nonvanishing component is

$$E_x = \frac{1}{\mu_e \sigma} \frac{dB_z}{dy} + wB_o. \tag{8}$$

The first two of the Maxwell equations indicate that $dE_x/dy = 0$. Therefore E_x is a constant. Integration of Eq. (6c) yields

$$\frac{1}{\mu_e \sigma} \frac{dB_z}{dy} + wB_o = C_5.$$

Comparison with Eq. (8) indicates that C_5 is the constant electric field E_x.

The velocity field can be calculated from the Momemtum Equation. By assumptions (1) and (2) from page 12, the left-hand side of Eq. (4) vanishes; therefore,

$$-\frac{\partial p}{\partial x} = 0; \tag{9a}$$

$$\frac{\partial p}{\partial y} + \frac{B_z}{\mu_e} \frac{\partial B_z}{\partial y} = 0; \tag{9b}$$

$$-\frac{\partial p}{\partial z} - \rho g + \frac{B_o}{\mu_e} \frac{\partial B_z}{\partial y} + \mu \frac{\partial^2 w}{\partial y^2} = 0. \tag{9c}$$

Equation (9a) indicates that the pressure is constant in the x direction, while a hydrostatic pressure gradient across the channel is caused by the induced magnetic field B_z. Integration of Eq. (9b) yields

$$p + B_z^2/(2\mu_e) = C_6.$$

Since

$$B_z = 0 \ \text{at} \ y = 0,$$

C_6 is the pressure p_c at the center of the channel. Therefore,

$$p_c - p = B_z^2/(2\mu_e).$$

Equations (9c) and (6c) consist of a system of two equations for the two unknowns w and B_z; i.e.,

$$\frac{1}{\mu_e \sigma} \frac{d^2 B_z}{dy^2} + B_o \frac{dw}{dy} = 0; \tag{6c}$$

$$-\left(\frac{\partial p}{\partial z} + \rho g\right) + \frac{B_o}{\mu_e} \frac{dB_z}{dy} + \mu \frac{d^2 w}{dy^2} = 0. \tag{9c}$$

The boundary conditions are

$$w = 0 \text{ at } y = \pm b,$$

and

$$B_z = 0 \text{ at } y = 0.$$

Elimination of dB_z/dy from Eq. (9c) results in

$$-\left(\frac{\partial p}{\partial z} + \rho g\right) + \sigma B_o \left(E_x - w B_o\right) + \mu \frac{d^2 w}{dy^2} = 0. \tag{10}$$

Since

$$Ha^2 = \sigma b^2 B_o^2/\mu,$$

then the solution is

$$w = \left(\frac{E_x}{B_o} - \frac{1}{\sigma B_o^2} \frac{\partial p}{\partial z} - \frac{1}{\sigma B_o^2} \rho g\right) \left(1 - \frac{\cosh[Ha(y)/b]}{\cosh Ha}\right). \tag{11}$$

From Eq. (8),

$$\frac{dB_z}{dy} = \sigma \mu_e (E_x - w B_o).$$

If Eq. (11) is substituted into the above equation and the result is integrated, the expression for B_z becomes

$$B_z = \mu_e \left[\frac{1}{B_o}\left(\frac{\partial p}{\partial z} + \rho g\right)y + \frac{b}{B_o Ha}\left(\sigma B_o E_x - \frac{\partial p}{\partial z} - \rho g\right) \frac{\sinh[Ha(y)/b]}{\cosh Ha}\right]. \tag{12}$$

From Eq. (7),

$$j_x = \frac{1}{\mu_e} \frac{dB_z}{dy}.$$

Differentiation of Eq. (12) yields

$$j_x = \frac{1}{B_o} \left(\frac{\partial p}{\partial z} + \rho g \right) + \frac{1}{B_o} \left(\sigma B_o E_x - \frac{\partial p}{\partial z} - \rho g \right) \frac{\cosh[Ha(y)/b]}{\cosh Ha}. \qquad (13)$$

The mass flow rate is

$$M = 2a\rho \int_{-b}^{+b} w \, dy.$$

Since $M/4ab\rho$ is the mean velocity U_m, when Eq. (11) for w is substituted into the above equation for mass flow rate and the result is integrated, the expression for U_m becomes

$$U_m = \left(\frac{E_x}{B_o} - \frac{1}{\sigma B_o^2} \frac{\partial p}{\partial z} - \frac{1}{\sigma B_o^2} \rho g \right) 1 - \frac{\tanh Ha}{Ha}. \qquad (14)$$

The total current I_x is

$$I_x = \int_{-b}^{+b} \int_0^L j_x \, dy \, dz.$$

Substituting Eq. (13) for j_x into the above equation and integrating give

$$I_x = \frac{2bL}{B_o} \left[\left(\frac{\partial p}{\partial z} + \rho g \right) + \frac{1}{Ha} \left(\sigma B_o E_x - \frac{\partial p}{\partial z} - \rho g \right) \tanh Ha \right].$$

Elimination of $(\partial p/\partial z) + \rho g$ by means of Eq. (14) yields

$$I_x = 2bL\sigma(E_x - U_m B_o). \qquad (15)$$

Eq. (15), the integrated form of Ohm's law, indicates that the current generated is independent of the detailed velocity distribution.

For simplicity, the ideal case is considered; namely, the walls are not conducting and there are no losses. To determine the electric field intensity E_x, the external load must be specified. Let R_o be the external load, and R_i the internal resistance. For the ideal case, the internal resistance is that of the fluid; thus,

$$R_i = 2a/2bL\sigma = a/bL\sigma.$$

Kirchoff's law requires that the generated emf, which is $2aU_mB_o$, be equal to the total IR loss of the circuit; thus,

$$\int_{+a}^{-a} U_mB_odx = I_x(R_o + R_i);$$

$$I_x = -\frac{2aU_mB_o}{R_o + R_i}. \tag{16}$$

Substitution of Eq. (16) into Eq. (15) yields

$$E_x = \left(1 - \frac{R_i}{R_o + R_i}\right)U_mB_o. \tag{17}$$

The power output P_o is

$$P_o = I_x \int_{+a}^{-a} E_xdx = \left(\frac{4a^2U_m^2B_o^2}{R_i}\right)\left[\frac{1}{1 + R_o/R_i}\right]\left[1 - \frac{1}{1 + R_o/R_i}\right]$$

$$= 4abL\sigma B_o^2U_m^2 \frac{R_o/R_i}{(1 + R_o/R_i)^2}. \tag{18}$$

When the gravitational force is neglected, the pressure drop from Eq. (14) becomes

$$-\frac{\partial p}{\partial z} = \sigma B_o^2U_m\left[\frac{Ha}{Ha - \tanh Ha} - \frac{1}{1 + R_i/R_o}\right]. \tag{19}$$

The total pressure drop Δp is thus

$$-\Delta p = -\frac{\partial p}{\partial z}L = \sigma B_o^2LU_m\left[\frac{Ha}{Ha - \tanh Ha} - \frac{1}{1 + R_i/R_o}\right]. \tag{20}$$

The required power for the flow is

$$P_p = 4abU_m(-\Delta p) = 4abL\sigma B_o^2U_m^2\left[\frac{Ha}{Ha - \tanh Ha} - \left(1 + \frac{R_i}{R_o}\right)^{-1}\right]. \tag{21}$$

The efficiency ϵ is

$$\epsilon = \frac{P_o}{P_p} = \frac{(R_o/R_i)(Ha/\tanh Ha - 1)}{(R_o/R_i + 1)(R_o/R_i + Ha/\tanh Ha)} \tag{22}$$

For a liquid metal generator,

$$Ha \gg 1$$

and

$$\frac{Ha}{Ha - \tanh Ha} \doteq 1.$$

Then

$$-\Delta p \doteq \sigma B_o^2 L U_m \left[1 - (1 + R_i/R_o)^{-1} \right] = \sigma B_o^2 L U_m (1 + R_o/R_i)^{-1}, (20a)$$

and

$$\epsilon \doteq \frac{R_o/R_i}{R_o/R_i + 1}. \tag{22a}$$

The foregoing analysis was for an ideal generator. In addition to the assumptions stated, additional inherent assumptions are that the walls are perfect insulators, no contact resistance exists between the fluid and the electrode, and there are no end losses due to end-current loops. For the ideal generator, the voltage between the two electrodes is obtained by integrating Eq. (17). That is,

$$V = \int_{-a}^{+a} \left[1 - \left(\frac{R_i}{R_o + R_i} \right) \right] U_m B_o dx. \tag{23}$$

By definition,

$$\gamma = R_o/R_i, \tag{24}$$

and

$$\eta = \text{loading factor} = \frac{\gamma}{1 + \gamma} = \frac{V}{2aU_m B_o} = \frac{\text{terminal voltage}}{\text{induced emf}}. \tag{25}$$

Therefore,

$$V = 2a\eta U_m B_o. \tag{26}$$

Similarly, it can be shown that the total current is

$$I = 2bL(1 - \eta)\sigma U_m B_o; \tag{27}$$

therefore,

$$P_g = VI = 4abL\eta(1 - \eta)\sigma U_m^2 B_o^2. \tag{28}$$

The electrical load is conveniently characterized by the external resistance R_o as follows:

$$R_o = \frac{V}{I} = \frac{2a\eta U_m B_o}{2bL(1-\eta)\sigma U_m B_o} \tag{29}$$

$$= \frac{\eta}{1-\eta}\frac{2a}{2bL\sigma}. \tag{30}$$

Since

$$\frac{2a}{2bL\sigma} = R_i, \qquad \gamma = \frac{\eta}{1-\eta}. \tag{31}$$

From Eq. (20a), the pressure drop across the channel is

$$-\Delta p = (1-\eta)L\sigma U_m B_o^2. \tag{32}$$

B. The Nonideal Generator

For the nonideal generator, three additional factors must be included to make the analysis applicable to the uncompensated experimental generator studied in this investigation. The first factor is the end effect produced by shunting the generator output by the fluid upstream and downstream from the electrodes; the second is the loading introduced by the conducting walls; the third is the reaction magnetic field developed in the direction of the applied field. In addition, allowance must be made for constant resistance between the working fluid and the generator duct walls.

1. End Losses

The end-loss problem was studied by Sutton et al.[13] for various electrode and magnetic field configurations, and with the assumption of small magnetic Reynolds number. For the case in which the magnetic field terminates at the end of the electrodes and with an aspect ratio greater than about 0.3, the following results were given:

$$V = \eta'(2a)U_m B_o; \tag{33}$$

$$V_{oc} = 2aU_m B_o[1+(2\ln 2)/c\pi]^{-1} \tag{34}$$

$$c = L/(2a) = \text{aspect ratio};$$

$$I = 2bL\sigma U_m B_o\{1-\eta'[1+(2\ln 2)/c\pi]\}. \tag{35}$$

Upon comparison of Eqs. (35) and 27), it is apparent that $(2\ln 2)/c\pi$ is a term which corrects for the end losses, and η' defines the new loading factor for the nonideal generator. It can be shown from circuit analysis that the end loss is equivalent to a shunt resistance R_e whose magnitude is

$$R_e = R_i \left(\frac{c\pi}{2 \ln 2} \right).$$

As the aspect ratio increases, this term becomes negligible and the above equations should become identical to the ideal case.

The value of η' is obtained as before.

$$R_o = \frac{\eta'(2a)U_m B_o}{2bL\sigma U_m B_o \{1 - \eta' [1 + (2 \ln 2)/c\pi]\}}$$

$$= \frac{\eta' R_i}{1 - \eta' [1 + (2 \ln 2)/c\pi]}. \qquad (36)$$

Therefore,

$$\eta' = \left(\frac{1}{\gamma} + 1 + \frac{2 \ln 2}{c\pi} \right)^{-1} = \left(\frac{R_i}{R_o} + 1 + \frac{2 \ln 2}{c\pi} \right)^{-1}. \qquad (37)$$

Similarly, it can be shown that for an exponential decay in field strength the loading factor is

$$\eta'' = \frac{1 + (2\beta_1/c\pi)}{1/\gamma + 1 + [(2 \ln 2)/c\pi]}, \qquad (38)$$

where β_1 is a factor defined by Sutton et al.[13] which accounts for the increase in electrode current due to the extension of the magnetic field. When c is very large, the end losses become negligible and

$$\eta' = (1/\gamma + 1)^{-1} = \eta. \qquad (39)$$

When $R_o = \infty$, i.e., $I = o$ (open circuit),

$$\eta' = [1 + (2 \ln 2)/c\pi]^{-1}, \qquad (40)$$

and

$$V = \frac{2aU_m B_o}{1 + [(2 \ln 2)/c\pi]} = V_{oc}. \qquad (41)$$

The pressure drop across the flow channel is

$$-\Delta p = (1 - \eta')L\sigma U_m B_o^2. \qquad (42)$$

2. Wall Effects

The wall effects are determined by simple circuit analysis. With reference to Fig. 4,

R_i = internal resistance of the generator

= resistance of NaK inside the channel

$$= \frac{2a}{2bL\sigma} = \frac{(2.16)(2.54)(42)}{(4)(2.54)(0.27)(2.54)(10^6)} = 33.7 \times 10^{-6} \text{ ohm;}$$

R_c = contact resistance between NaK and electrodes;

R_w = measured wall resistance = 431.8×10^{-6} ohm;

R_{BB} = bus-bar resistance between measuring points 1-1' and 2-2';

R_{sh} = shunt resistance used for measuring current;

R_{ss} = fixed resistance as a part of load.
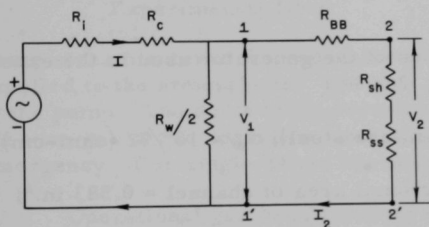
Fig. 4

Electrical Circuit of Experimental MHD Generator and Load

The series combination of the three external loads R_{BB}, R_{sh}, and R_{ss} is in parallel with the wall resistance R_w and forms a combined external resistance. This is in series with the contact resistance between the electrode and the fluid, and forms a combined external resistance R_o. That is,

$$R_o = R_c + \left(\frac{2}{R_w} + \frac{1}{R_{BB} + R_{sh} + R_{ss}} \right)^{-1}. \tag{43}$$

3. Reaction Magnetic Field

The analysis presented thus far is for a compensated generator. The generator studied in this experiment was, in a sense, almost totally compensated, since the major portion of the current flowed through the generator walls. Also, it can be shown that for a low magnetic Reynolds number ($R_m < 1$), the induced field and its resultant effect are negligible.

Therefore, the general expressions for the nonideal generator (used in this investigation) become

$$V = 2aU_mB_o \bigg/ \left[1 + \frac{2 \ln 2}{c\pi} + \frac{R_i(R_w + 2R_o')}{R_c(R_w + 2R_o') + R_o'R_w} \right], \tag{44}$$

$$I = 2bL\sigma U_mB_o \; \frac{R_i(2R_o' + R_w)}{R_i(2R_o' + R_w) + \left(1 + \dfrac{2 \ln 2}{c\pi}\right)(2R_o'R_c + R_wR_c + R_wR_o')}, \tag{45}$$

and

$$-\Delta p = \sigma L U_m B_o^2 \; \frac{\dfrac{2 \ln 2}{c\pi} + \dfrac{R_i(R_w + 2R_o')}{R_c(R_w + 2R_o') + R_o'R_w}}{1 + \dfrac{2 \ln 2}{c\pi} + \dfrac{R_i(R_w + 2R_o)}{R_c(R_w + 2R_o') + R_o'R_w}}, \tag{46}$$

where

$$R_o' = R_{sh} + R_{ss} + R_{BB}.$$

The pertinent dimensions of the generator used in the experimental investigation were (see Fig. 2)

Wall thickness = $\frac{1}{32}$ in. (stainless steel); $\sigma_w = 10^6/72$ (ohm-cm)$^{-1}$;

$4ba$ = cross-sectional area of channel = 0.583 in.^{2};

$2a$ = 2.16 in.;

$2b$ = 0.27 in.;

L = length of electrode = 4 in.

The magnetic field terminates at the ends of electrodes.

The characteristics of conducting fluid NaK (at 75°F) are

μ = 1.6 lb/(hr)(ft);

ρ = 54.3 lb/ft^3;

σ = 10^6/42 (ohm-cm)$^{-1}$.

During the experimental investigation, data were taken in four series of tests. The conditions for each series resulted in different total external and internal load factors, which altered the performance characteristics of the generator. A detailed analysis of each test series is given in Section IV.

III. LABORATORY APPARATUS AND EXPERIMENTAL PROCEDURE

A. General

The experimental investigation was conducted on a basic NaK test loop which is schematically illustrated in Fig. 5. The loop was constructed from 2-in., Schedule 40, stainless steel pipe, and all individual components were of a welded design. All valves were made from stainless steel and were of a bellows seal-globe type.
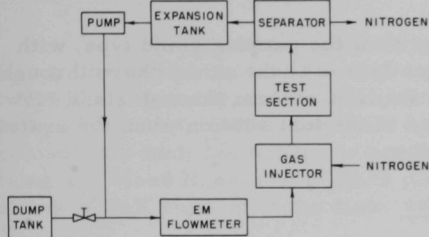
Fig. 5. Schematic Diagram of Experimental Loop

The loop could be operated with either NaK or an NaK-N_2 mixture. When operating with a two-phase mixture, metered streams of NaK and dry nitrogen were combined in the mixing section. After passing through the test section, the two-phase stream entered the separator where the nitrogen was removed and expelled to the atmosphere. The NaK flowed to the expansion tank and on to the pump. The dump tanks served as storage tanks for the NaK when the loop was not in operation, and as a safety feature in the event of an emergency. For single-phase operation, the nitrogen flow was discontinued.

Operational gas requirements were met by three independent nitrogen systems: one to supply nitrogen to the gas injector; one to provide for the shaft-sealing arrangement on the pump; and one to provide a blanket gas for the system and to pressurize the dump tanks to fill the system.

B. Loop Components

1. NaK Pump

The NaK pump, shown schematically in Fig. 6, was of the vertically mounted centrifugal type, driven directly by a three-phase, $\frac{3}{4}$-horsepower motor.
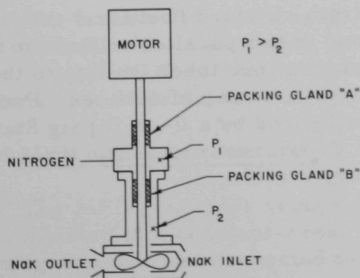
Fig. 6

Schematic Diagram of NaK Pump

NaK leakage was prevented by maintaining a 0.5- to 1-psi pressure differential between the high- and low-pressure sections of the specially-designed gas seal. The low pressure was that of the system blanket gas, approximately 1 psig. The high and low pressures, as well as the breather tank pressure and dump tank pressure, were read on compound Bourdon gages which had been calibrated against a mercury manometer.

Shaft seals "A" and "B" were of the packing gland type, with an asbestos-graphite packing. Nitrogen leaked to the atmosphere through gland "A". The introduction of gas to the NaK stream through gland "B" was negligible. No voids were detected in the test section when the system was operated with single-phase NaK flow.

2. Electromagnetic Flowmeter

An electromagnetic flowmeter was constructed by mounting a permanent magnet on a section of straight pipe and welding two electrodes to the pipe, so that the electrodes were perpendicular to the pipe and to the magnetic field.

The output of the flowmeter was fed through a ten-to-one amplifier to a Brown recorder which was equipped with a 0- to 10-mV bucking voltage. The flowmeter was calibrated against an orifice introduced in the system specifically for this purpose. Calibrations on two separate occasions over different flow ranges yielded the expected linear relationship of flowmeter output versus flow rate.

3. Gas Injector and Supply

The gas injector consisted of a short length of perforated 2-in. stainless steel pipe surrounded by a concentric length of 5-in. pipe. The annulus was blanked off at each end.

Nitrogen entered the annulus through four radially-spaced, $\frac{1}{4}$-in. stainless steel tubes, and merged with the vertically-flowing NaK stream through 165 holes spaced around and along the inner pipe.

The gas was supplied from standard "bottles," through a drier and filter, and then through one of two parallel orifices to a manifold which distributed the nitrogen to the four tubes leading to the injector. The gas flow was metered by means of a series of orifices. Pressure drop across the gas orifices was measured by a 0- to 5-psig Statham transducer; the output was fed to a Brown recorder. The transducer was initially calibrated against a mercury manometer.

4. NaK-N₂ Separator

The separator consisted of a cylindrical tank mounted at a slight angle to the horizontal. The capacity of the tank was large enough to permit the incoming two-phase mixture to decrease in velocity and thus allow the gas to escape. The nitrogen traveled along the top of the cylindrical tank and up the breather pipe to the breather tank where it was bled to the atmosphere.

The breather tank was provided with a pressure-equalizing line to the expansion tank to maintain a relatively constant NaK level between the separator and the expansion tank. A drain line was added to the expansion tank to collect any NaK carryover by the breather pipe. Other components included baffles to prevent NaK from splashing into the equalizing and bleed lines, and a spark plug-type level indicator to trip an alarm if NaK built up in the tank.

5. Expansion Tank

The expansion tank was located in the flow path between the separator and the pump. NaK entered the bottom of the tank, passed around baffles to prevent splashing, and continued to the pump through an outlet at the rear. Observation ports provided visual indication of liquid level during loop operation and when the system was being filled.

Three $\frac{1}{4}$-in. pipe lines entered the top of the tank as follows: (1) a line to the system blanket gas supply; (2) a drain line from the breather tank; and (3) a pressure-equalizing line to the breather tank. Any gas not removed by the separator could have been removed in the expansion tank, where it would be passed through the equalizing line to the breather tank.

6. Dump Tanks

The dump tanks had a capacity of approximately 40 gallons. They were used to store the NaK when the loop was not in operation, and as a safety feature in the event of an emergency. The loop was filled by pressurizing the tanks with nitrogen.

The tanks also served as an oxide-purging system. The oxides that formed in the NaK during operation tended to collect in the dump tanks. As the NaK was returned to the storage tanks after each series of runs, the oxide deposits accumulated at the surface in the tanks.

7. MHD Generator Section

The MHD generator section is illustrated schematically in Fig. 7. It consisted of a constant-area, rectangular channel installed between the magnet poles and connected to the loop by gradual contraction

28

Fig. 7. Schematic Diagram of MHD
Generator Section

2-in. SST PIPE

POLES: 2-7/16 x 4

2-1/8

1/4

B_0

B_0

5-1/4

4

32-5/8

FLOW
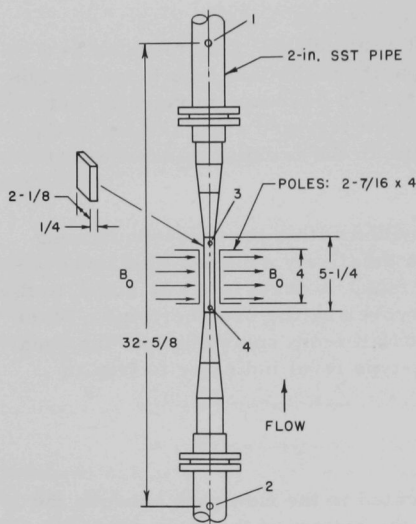
NOTE: ALL DIMENSIONS IN INCHES

and expansion sections. The channel was fabricated from 0.031-in.-thick stainless steel plate, with inside dimensions of 0.27 x 2.16 in. Points 1, 2, and 3 indicate the positions of pressure taps relative to the magnetic field. Void fraction measurements were taken above and below the magnetic field in the constant-area, rectangular channel. Pressure taps 3 and 4 were located 2 in. upstream and downstream, respectively, of the field poles to measure the total effect of the magnetic field. Figure 8 shows the generator test section, the electromagnet, and the photomultiplier tube assembly.

The magnet was series-wound with windings of $\frac{1}{4}$- x 4-in. copper bus bar. Connections with the power supply were also made with $\frac{1}{4}$- x 4-in. copper bus bar. Pole faces were $2\frac{7}{16}$ x 4 in., with a $\frac{3}{8}$ in. gap.

NaK CHANNEL

BUS BAR

ELECTROMAGNET

PRESSURE TAP

ELECTRODE

PM TUBE ASSEMBLY
ON TRAVERSING PLATFORM

112-3496

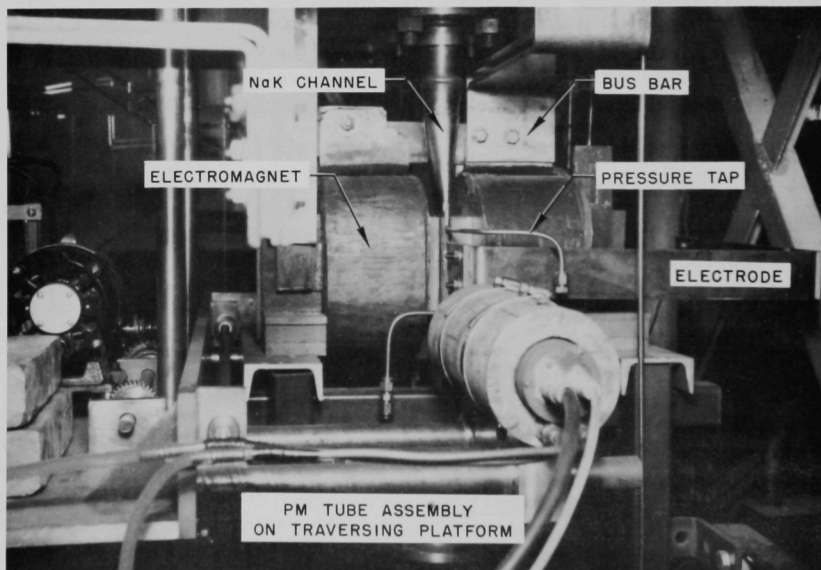Fig. 8. MHD Generator Section, Electromagnet, and Photomultiplier Tube Assembly

Power for the D-C electromagnet was supplied by a three-phase, 440-volt rectifier with a maximum output of 3000 Amp at 2 V. Current output was controlled with a "stepper-switch" on the power supply. This resulted in current being available at certain discrete values which could be obtained consistently and which remained relatively constant during each test run. Current output was determined by measuring the potential drop across a known shunt resistance with a Brown recorder.

Before the test section was placed in the loop, a curve of average magnetic field strength versus current input was determined with a Gaussmeter (a direct-reading, transistorized instrument which operated on the Hall effect principle and had a range of 50 kilogauss). The probe used to determine the field strength was initially calibrated against a 1000-Gauss reference magnet. Field strength was recorded at 24 points over the area of the pole face and midway between the poles. The field was essentially uniform across the pole. This is well within the accuracy of the determination because of the criticality of the angle of the face of the probe with respect to the pole face. Fringing effects could not be determined accurately because of the finite size of the probe. However, indications were that the field strength fell off rapidly. Therefore, the assumption of a uniform field with abrupt edges was considered to be justified.

The pressure drop across the generator section was measured by either a ±1- or a ±15-psi Statham transducer, depending upon test conditions. The transducers were initially calibrated against a water manometer and a mercury manometer, respectively. Transducer output was read on a Brown recorder.

Because of the hazards posed by bleeding NaK to the atmosphere, and because of the problems which would be encountered if NaK had to be removed from the transducer, the system of pots shown in Fig. 9 was devised. NaK was bled from the pressure taps into the pots which contained kerosene. When the system was in operation, pressure was transmitted through the NaK-kerosene interfaces in the pots to the transducer.
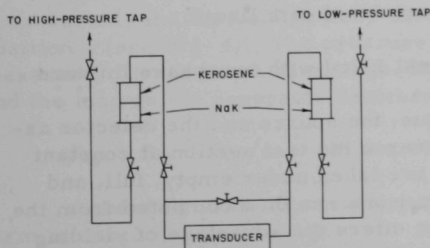

Fig. 9

System for Measuring Pressure Drop in Test Section

The pots were constructed from 2-in. Pyrex pipe fittings; the ends were blanked off with stainless steel plates and sealed with Buna N O-rings. Stainless steel tubing (0.25-in. O.D.) was used to interconnect the pressure taps, pots, and transducer. Needle valves with asbestos-graphite packing were used in the NaK lines; Teflon-packed valves were installed in the kerosene lines.

The void fraction before and after the magnetic field in the generator section was determined by the gamma-ray attenuation technique.[14,15] Essentially, the technique consists of placing a gamma-ray source on one side of the test section, and a collimator, scintillation crystal, and photomultiplier tube on the other. The output of the tube is a function of the unattenuated portion of the gamma rays. The source was thulium-170 rated at about 20 r/hr at a distance of 2 in. The output of the photomultiplier tube was fed through a current amplifier to a Brown recorder.

Initially, measurements were made by the "one-shot" technique to obtain some idea of the effect of the magnetic field on the void fraction. Later, the more accurate traversing technique was employed.

In the "one-shot" method, the source and the photomultiplier tube assembly are stationary with respect to, and centered on the test section. A collimator with a window slightly wider than the width of the channel is employed. The average void fraction is determined from the relation

$$\alpha = \ln(V_o/V_f)/\ln(V_e/V_f),$$

where

α = void fraction;

V_e = output voltage for empty channel;

V_f = output voltage for channel filled with liquid;

V_o = output voltage for channel filled with two-phase mixture.

In the traversing technique, the source and the detector assembly with a narrow collimator traverse the test section at constant speed. Traces of the voltage output are taken under empty, full, and two-phase conditions. Local void fractions are then computed from the relation shown above. This technique offers the advantage of yielding the void distribution across the channel. Average void fractions are determined by numerical integration.

IV. DISCUSSION OF RESULTS

The data were obtained in four series of tests: (1) NaK flowing through the generator with an open circuit (no external loads); (2) NaK flowing through the loaded generator; (3) NaK-N_2 flowing through the generator with an open circuit; and (4) NaK-N_2 flowing through the loaded generator. The open-circuit condition is not a true open circuit, since the walls of the generator are conducting and, therefore, a net current flow exists even though the external loop is open.

Before the experimental investigation was started, tests were made to establish the effective wall resistance, since the generator walls were conducting. A voltage was applied across the generator, and the current was measured. The resistance was then computed. The contact resistance between the wall and the NaK was assumed to be zero. This assumption was based on experience with electromagnetic pumps where this condition was ultimately achieved after prolonged recirculation. The computed values were

$$R_w = 431.8 \times 10^{-6} \text{ ohm};$$

$$R_c = 0 \text{ ohm}.$$

The combined external load resistance was determined to be

$$R_{sh} + R_{ss} = 1306.1 \times 10^{-6} \text{ ohm};$$

$$R_{BB} = 93 \times 10^{-6} \text{ ohm}.$$

The measured and calculated resistances were used in conjunction with Eqs. (44), (45), and (46) to calculate the theoretical generator performance. The theoretical performance characteristics of the generator are compared with the data in the following paragraphs.

A. Test Series I: NaK (Open Circuit)

In this test series, the NaK flow rate and the magnetic field intensity were varied, and the voltage drop across the generator was measured at position 1 (see Fig. 4). The pressure drop across the generator was also measured. Under these conditions, R_{BB}, R_{sh}, and R_{ss} are set equal to ∞, and the load on the generator becomes

$$R_o = R_c + R_w/2 = 215.9 \times 10^{-6} \text{ ohm}. \tag{47}$$

According to the dimensions of the generator, the end-loss correction term is

$$\frac{2 \ln 2}{c \pi} = \frac{2 \ln 2}{4 \pi / 2.16} = 0.239.$$

The voltage V_1 which corresponds to the position of measurement becomes

$$V_1 = V - IR_c$$

$$= V - R_c(2V_1/R_w)$$

$$= [1 + (2R_c/R_w)]^{-1}V. \tag{48}$$

Substituting in Eq. (48) with R_o given by Eq. (47) produces

$$V_1 = 2aU_mB_o \Big/ \left(1 + \frac{2R_c}{R_w}\right)\left[\frac{R_i}{R_c + (R_w/2)} + 1 + \frac{2 \ln 2}{c\pi}\right]. \tag{49}$$

Substituting the values for the resistances in Eq. (49) produces

$$V_1 = \frac{2aU_mB_o}{1.395} \text{ (with end-loss correction)}, \tag{50}$$

and

$$V_1' = \frac{2aU_mB_o}{1.156} \text{ (without end-loss correction)}. \tag{51}$$

The loading factor is given by

$$\eta' = [1 + (R_i/R_o) + 0.239]^{-1} = 0.717 \text{ (with end-loss correction)};$$

$$\tag{52}$$

$$\eta = [1 + (R_i/R_o)]^{-1} = 0.865 \text{ (without end-loss correction)}. \tag{53}$$

The voltages computed from Eqs. (50) and (51) are compared with the experimental data in Figs. 10, 11, 12, and 13. The calculated values are represented by the solid and dashed curves; the latter indicate that the end losses have been neglected. As can be seen, the agreement between data and theory which takes into consideration the end losses is excellent. Thus the use of the end-loss factor $(2 \ln 2)/c\pi$ recommended by Sutton for an abrupt termination of the magnetic field at the electrode end appears to be valid and quite accurate. (The applied magnetic field across the generator did terminate abruptly.) On the other hand, comparison of the data with the loading factor derived for an exponential field decay, Eq. (38), indicates further deviation from the calculated values. This is shown in Fig. 10 for $B_o = 8800$ Gauss. When the end losses are neglected, the measured voltage drop is about 15-20% below the calculated values. The slight deviation of the data points at low Gauss field and high NaK flow rates is because the magnetic field was not stabilized and because of the sequence in which the data were taken. Initial tests were made when the NaK flow rate was at a maximum and the initial magnet temperature was at a minimum. As the test

sequence progressed, the temperature of the magnet winding increased and therefore the magnetic field strength decreased slightly. Eventually, the magnet temperature and field strength stabilized, and this value is the one listed on the figures. The magnetic field is actually slightly higher for the high-flow data points, and this is thought to be the reason for the slight deviation.
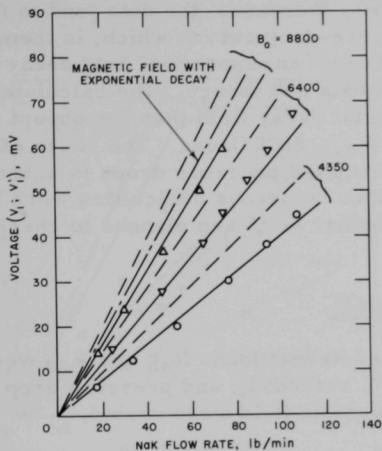

Fig. 10. Comparison of Calculated and Measured Voltage; Test Series I: B_0 = 8800, 6400, and 4350 Gauss

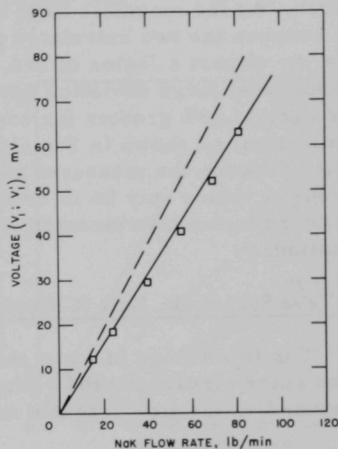

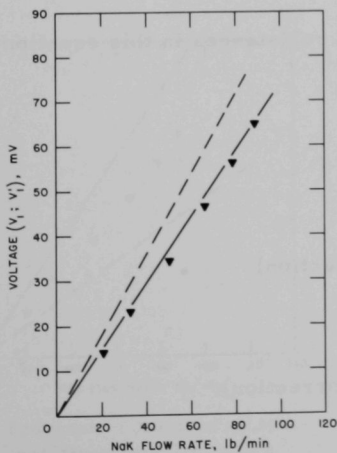Fig. 11. Comparison of Calculated and Measured Voltage; Test Series I: B_0 = 8450 Gauss

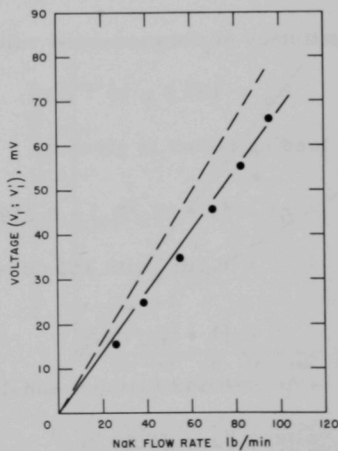Fig. 12. Comparison of Calculated and Measured Voltage; Test Series I: B_0 = 7940 Gauss

Fig. 13. Comparison of Calculated and Measured Voltage; Test Series I: B_0 = 7320 Gauss

The pressure drop was computed by substituting into Eq. (42) the value of η' and η given by Eqs. (52) and (53). The calculated and the measured pressure drops are compared in Figs. 14 to 17. The dashed curve represents the calculated pressure drop without the end-loss factors. As can be seen, the data lie near the calculated pressure drop that incorporates end-loss factors. As the magnetic field intensity increases, the data tend to fall midway between the two calculated pressure-drop curves which, in themselves, differ by almost a factor of two. The use of an exponential field decay causes an additional large deviation between data and theory. The calculated pressure drop is 18% greater for exponential decay field than for abrupt field termination, as shown in Fig. 14 for B_0 = 8800 Gauss. The cause of the deviation between the measured and calculated pressure drops is unknown. The measured values may be in error, since numerous difficulties were encountered in the instrumentation. Further tests are planned to check out the deviation.

B. Test Series II: NaK (Closed Circuit)

In this series of runs, the two external loads R_{sh} and R_{ss} were placed in the outer circuit and the voltage V_2, current I_2, and pressure drop were measured as the flow rate and the magnetic field were varied.

With reference to the circuit diagram (Fig. 4), the external load is

$$R_o = R_c + \left(\frac{2}{R_w} + \frac{1}{R_{BB} + R_{sh} + R_{ss}} \right)^{-1}.$$

Substitution of the measured values of resistances in this equation yields

$$R_o = 187.3 \times 10^{-6} \text{ ohm}.$$

The loading factor is given by

$$\eta' = [1 + (R_i/R_o) + 0.239]^{-1}$$

$$= 0.705 \text{ (with end-loss correction);} \tag{54}$$

$$\eta = [1 + (R_i/R_o)]^{-1}$$

$$= 0.848 \text{ (without end-loss correction).} \tag{55}$$

The voltage V_2 is given by

$$V_2 = V_1 \left(\frac{R_{sh} + R_{ss}}{R_{BB} + R_{sh} + R_{ss}} \right),$$

where

$$V_1 = V - IR_c = \eta'(2a)U_m B_0 - (2I_w + I_2)R_c$$

$$= \eta'(2a)U_m B_0 - \left[\frac{2}{R_w} + \frac{1}{R_{BB} + R_{sh} + R_{ss}} \right] V_1 R_c.$$

Fig. 14. Comparison of Calculated and Measured Pressure Drop; Test Series I: $B_0 = 8800$ and 6400 Gauss

Fig. 15. Comparison of Calculated and Measured Pressure Drop; Test Series I: $B_0 = 8450$ and 4350 Gauss

Fig. 16. Comparison of Calculated and Measured Pressure Drop; Test Series I: $B_0 = 7940$ Gauss

Fig. 17. Comparison of Calculated and Measured Pressure Drop; Test Series I: $B_0 = 7320$ Gauss

Therefore

$$V_2 = \left[\left(\frac{R_{sh} + R_{ss}}{R_{BB} + R_{sh} + R_{ss}}\right)\middle/\left(1 + \frac{2R_c}{R_w} + \frac{R_c}{R_{BB} + R_{sh} + R_{ss}}\right)\right]$$

$$x \, (2a \, \eta' U_m B_o). \tag{56}$$

Substituting the numerical values of the resistances in Eq. (56) yields

$$V_2 = \frac{2aU_m B_o}{1.522} \text{ (with end-loss correction);} \tag{57}$$

$$V_2' = \frac{2aU_m B_o}{1.266} \text{ (without end-loss correction).} \tag{58}$$

The data for the closed-circuit condition and Eqs. (57) and (58) are compared in Figs. 18 to 21; the agreement is excellent. Again, when the end losses are excluded, the experimental data fall below the calculated values. As in Test Series I, a slight deviation at the higher flow rates is evident.
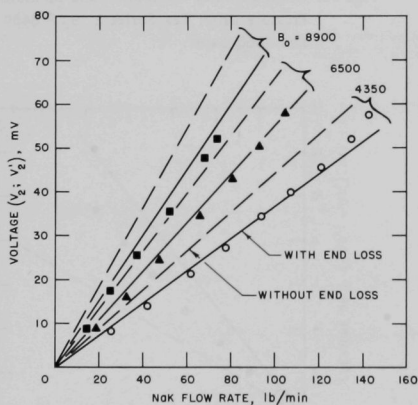
Fig. 18. Comparison of Calculated and Measured Voltage; Test Series II: $B_o = 8900$, 6500, and 4350 Gauss
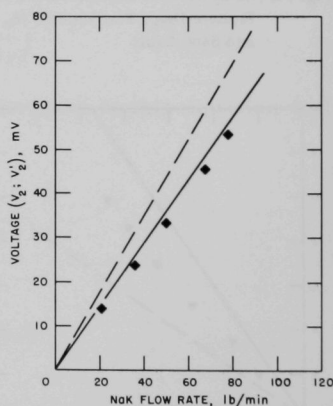
Fig. 19. Comparison of Calculated and Measured Voltage: Test Series II: $B_o = 8500$ Gauss
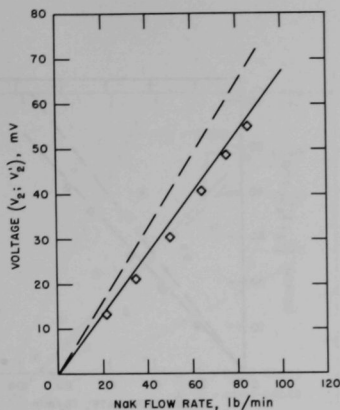
Fig. 20. Comparison of Cal-
culated and Meas-
ured Voltage; Test
Series II: B_O =
8000 Gauss
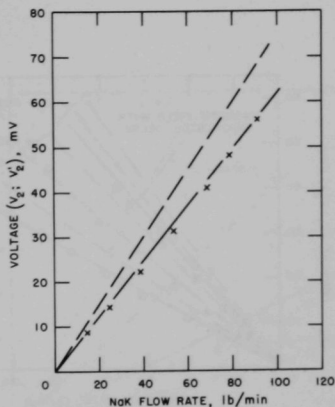
Fig. 21. Comparison of Cal-
culated and Meas-
ured Voltage; Test
Series II: B_O =
7350 Gauss

The current, I_2, was computed from the relationships

$$I_2 = \frac{V_2}{R_{sh} + R_{ss}} \text{ (with end-loss correction)};$$ (59)

$$I_2' = \frac{V_2'}{R_{sh} + R_{ss}} \text{ (without end-loss correction).}$$ (60)

A comparison between the calculated and measured current is shown in
Figs. 22 to 25; the agreement is good. If the exponential field decay is taken
into consideration, the measured current is about 17% below the calculated
values shown in Fig. 22 for B_O = 8900 Gauss.

The calculated and measured pressure drops are shown in Figs. 26
to 29.

The data from the first two series of runs indicate that modification
and extension of Hartmann's theory to the nonideal generator case does
predict generator performance accurately.
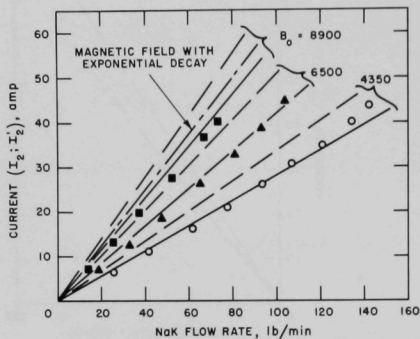
Fig. 22. Comparison of Calculated and Measured Current; Test Series II: B_O = 8900, 6500, and 4350 Gauss
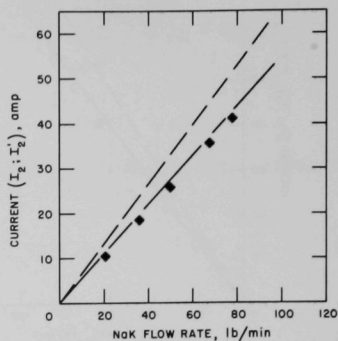
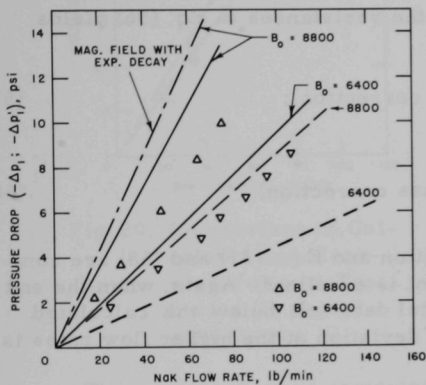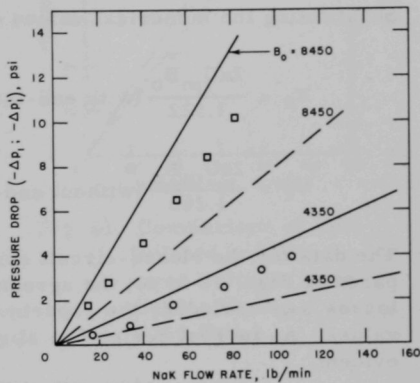Fig. 23. Comparison of Calculated and Measured Current; Test Series II: B_O = 8500 Gauss
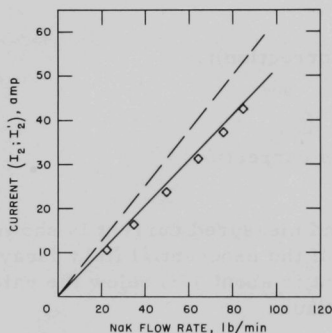
Fig. 24. Comparison of Calculated and Measured Current; Test Series II: B_O = 8000 Gauss
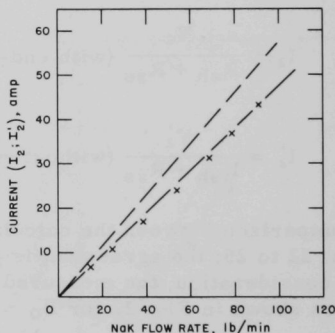
Fig. 25. Comparison of Calculated and Measured Current; Test Series II: B_O = 7350 Gauss
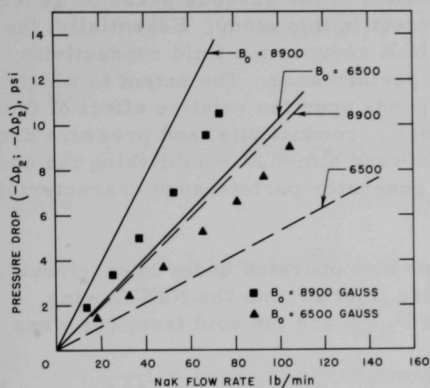
Fig. 26. Comparison of Calculated
and Measured Pressure
Drop; Test Series II:
B_O = 8900 and 6500 Gauss
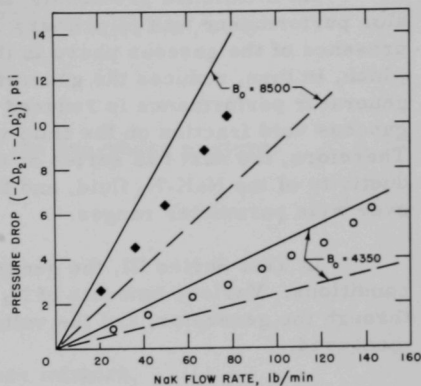
Fig. 27. Comparison of Calculated
and Measured Pressure
Drop; Test Series II:
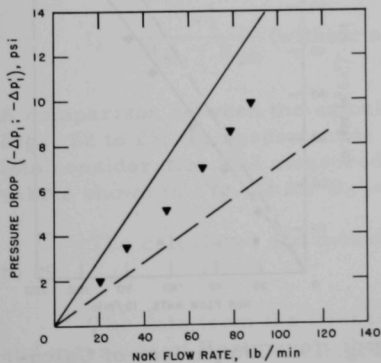B_O = 8500 and 4350 Gauss
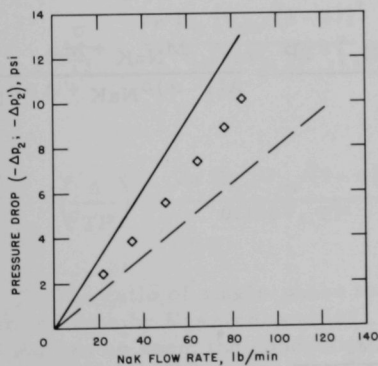
Fig. 28. Comparison of Calcu-
lated and Measured
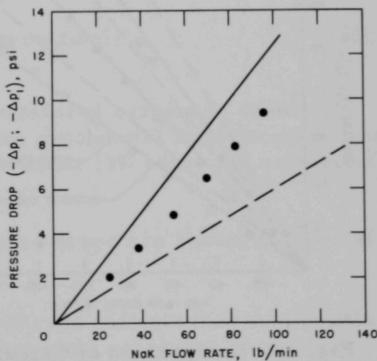Pressure Drop; Test
Series II: B_O =
8000 Gauss
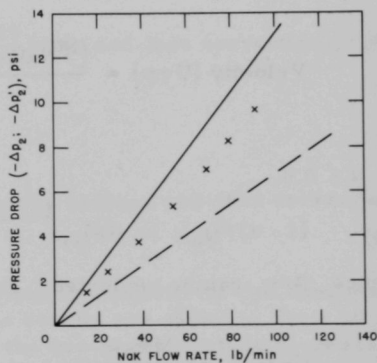
Fig. 29. Comparison of Calcu-
lated and Measured
Pressure Drop; Test
Series II: B_O =
7350 Gauss

C. Test Series III: NaK-N$_2$ (Open Circuit)

As mentioned previously, the effect of the gaseous phase on generator performance was of primary interest in this study. Essentially, the presence of the gaseous phase in the NaK reduces the fluid conductivity which, in turn, reduces the generator performance. The extent to which generator performance is reduced depends upon the relative effect of the gaseous void fraction on the fluid velocity, conductivity, and pressure drop. Therefore, the next two series of runs were aimed at establishing the conductivity of the NaK-N$_2$ fluid, and the generator performance characteristics over wide parameter ranges.

In Test Series III, the generator was operated under open-circuit conditions. Various amounts of N$_2$ were injected into the NaK flowing through the generator, and the voltage $V_{1,TP}$ and the void fractions were measured.

The NaK-N$_2$ mixture was considered to have the following properties:

$$\text{Density } (\rho_{TP}) = (1 - \alpha)\rho_{NaK} + \alpha\rho_{N_2}; \tag{61}$$

$$\text{Specific Volume } (v_{TP}) = \frac{1}{\rho_{TP}} = \frac{1}{(1 - \alpha)\rho_{NaK} + \rho_{N_2}}; \tag{62}$$

$$\text{Velocity } (U_{TP}) = \frac{\left(M_{NaK} + M_{N_2}\right)v_{TP}}{A} = \frac{M_{NaK} + M_{N_2}}{A(1 - \alpha)\rho_{NaK} + A\alpha\rho_{N_2}}. \tag{63}$$

If $\alpha < 0.9$,

$$(1 - \alpha)\rho_{NaK} \gg \alpha\rho_{N_2};$$

hence, $\alpha\rho_{N_2}$ can be neglected. Then,

$$U_{TP} = \frac{M_{NaK}}{A(1 - \alpha)\rho_{NaK}} + \frac{M_{N_2}}{A(1 - \alpha)\rho_{NaK}}.$$

In the present experiment,

$$M_{NaK} \gg M_{N_2};$$

therefore,

$$U_{TP} = \frac{M_{NaK}}{A(1 - \alpha)\rho_{NaK}} = \frac{U_m}{1 - \alpha}. \tag{64}$$

The voltage $V_{1,TP}$ is given by

$$V_{1,TP} = \frac{2aB_o\left[U_m/(1-\alpha)\right]}{\left[(1+2R_c/R_w)\right]\left\{R_{i,TP}/R_o + 1 + \left[(2\ln 2)/c\pi\right]\right\}}, \tag{65}$$

where

$R_{i,TP}$ = internal resistance of the two-phase mixture.

Since

$$R_{i,TP} = (\sigma/\sigma_{TP})R_i$$

and

σ_{TP} = conductivity of two-phase mixture,

it follows that

$$R_o = R_c + R_w/2 = 215.9 \times 10^{-6} \text{ ohm.}$$

Equation (65) can be simplified to give

$$\frac{\sigma}{\sigma_{TP}} = \frac{2a\,B_o\left[U_m/(1-\alpha)\right]}{0.156V_{1,TP}} - \frac{1.239}{0.156} \quad \text{(with end-loss correction);} \tag{66}$$

or

$$\left(\frac{\sigma}{\sigma_{TP}}\right)' = \frac{2a\,B_o\left[U_m/(1-\alpha)\right]}{0.156V_{1,TP}} - \frac{1}{0.156} \quad \text{(without end-loss correction).} \tag{67}$$

The ratio of single-phase to two-phase conductivity was computed from the data by Eqs. (66) and (67). The results are shown in Figs. 30 and 31. As can be seen, the conductivity of the two-phase mixture decreases rapidly as the void fraction increases. If the results shown in Fig. 30 are plotted on semi-logarithmic paper, a nearly straight line can be obtained. Hence, in the interval of $0.3 < (1-\alpha) < 1.0$, the two-phase conductivity may be represented by the relationship

$$\sigma/\sigma_{TP} = e^{3.8\alpha}. \tag{68}$$

Also shown in Fig. 30 is the equation proposed by Maxwell[16] for computing the effective conductivity for mixtures of fluids or powders. The original Maxwell equation is

$$\sigma' = \frac{2\sigma_2 + \sigma_1 - 2\alpha(\sigma_2 - \sigma_1)}{2\sigma_2 + \sigma_1 + \alpha(\sigma_2 - \sigma_1)} \sigma_2; \tag{69}$$

where

σ' = conductivity of the mixture,

α = ratio of the volume of the gas bubbles to that of the second medium,

σ_1 = conductivity of the discontinuous phase,

σ_2 = conductivity of the continuous phase.

If it is assumed that the gas bubbles are solid spheres with zero conductivity, and the fluid is a homogeneous mixture, Maxwell's equation reduces to

$$\sigma' = [2(1 - \alpha)\sigma_2]/(2 + \alpha). \tag{70}$$

This is the relationship plotted in Fig. 30. As can be seen, the deviation between the data and Eq. (70) is large. It is not surprising that the magnitude of the deviation is so large when the nature of the two-phase flow is compared to the assumption made by Maxwell in his derivation.
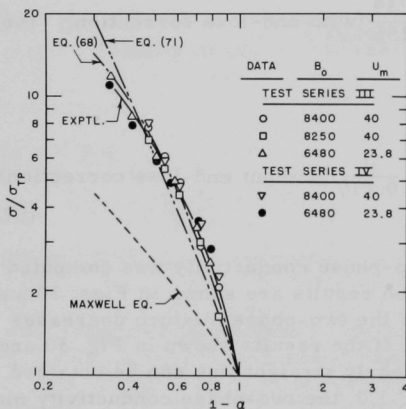
Fig. 30. Single-phase to Two-phase Conductivity Ratio versus Void Fraction, with End-loss Correction
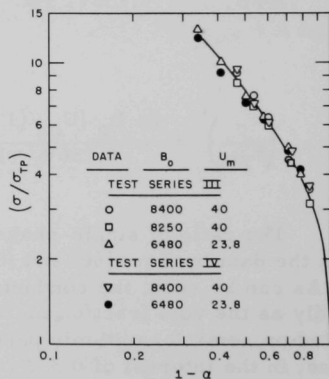
Fig. 31. Single-phase to Two-phase Conductivity Ratio versus Void Fraction without End-loss Correction

The two-phase conductivity data can also be approximated closely by the following simplified expression:

$$\sigma_{TP} = \sigma(1 - \alpha)^3/(1 - \alpha^2). \tag{71}$$

The results are also plotted in Fig. 30. Equation (71) was derived by utilizing data obtained on the effective conductivity of metal sheets with various perforations. It has been reported in the literature that the effective conductivity of the metal sheets can be correlated by the following expression:

$$\sigma_{eff} = \sigma(1 - \alpha)(1 + \alpha)^{-1} + K_1(\alpha). \tag{72}$$

The term $K_1(\alpha)$ was dropped since its magnitude was extremely small. The resistance of the NaK-N_2 mixture in the MHD channel is

$$R_{TP} = 2a/(\sigma_{TP} \cdot 2bL).$$

The resistance of NaK (mixing with N_2), by using Eq. (72), is

$$R_{NaK} = \frac{2a}{\sigma_{eff} \cdot 2bL(1 - \alpha)} = \frac{2a}{\sigma \cdot 2bL \ [(1 - \alpha)^2/(1 + \alpha)]}; \tag{73}$$

$$R_{TP} \doteq R_{NaK}.$$

Therefore,

$$\sigma_{TP} = \sigma[(1 - \alpha)^2/(1 + \alpha)]; \tag{74}$$

or, if the numerator and denominator are multiplied by $(1 - \alpha)$, the result is

$$\sigma_{TP} = \sigma[(1 - \alpha)^3/(1 - \alpha^2)]. \tag{75}$$

In the limit $\alpha \to 1$, the two-phase conductivity becomes zero.

D. Test Series IV: NaK-N_2 (Closed Circuit)

The final series of tests was made with the two-phase mixture flowing through the generator and the external resistances R_{BB}, R_{sh}, and R_{ss} in the circuit. Under these conditions the voltage is

$$V_{2,TP} = \left[\left(\frac{R_{sh} + R_{ss}}{R_{BB} + R_{sh} + R_{ss}} \right) \Big/ \left(1 + \frac{2R_c}{R_w} + \frac{R_c}{R_{BB} + R_{sh} + R_{ss}} \right) \right]$$

$$\times \left[\left(2aB_o \frac{U_m}{1 - \alpha} \right) \Big/ \left(\frac{R_{i,TP}}{R_o} + 1 + \frac{2 \ln 2}{c \pi} \right) \right]. \tag{76}$$

Since

$$R_{i,TP} = \frac{2a}{2bL\sigma_{TP}} = \frac{\sigma}{\sigma_{TP}} R_i,$$

Eq. (76) can be solved for the conductivity ratios

$$\frac{\sigma}{\sigma_{TP}} = \frac{0.932\ \{2aB_o[U_m/(1-\alpha)]\}}{0.180V_{2,TP}} - \frac{1.239}{0.180} \text{ (with end-loss correction);}$$

(77)

$$\left(\frac{\sigma}{\sigma_{TP}}\right)' = \frac{0.932\ \{2aB_o(U_m/1-\alpha)\}}{0.180V_{2,TP}} - \frac{1}{0.180} \begin{array}{l}\text{(without end-loss} \\ \text{correction).}\end{array}$$

(78)

The conductivity ratios were computed from Eqs. (77) and (78). The results are also shown in Figs. 30 and 31. As can be seen, there is excellent agreement between the ratios derived from the two series of runs.

E. Variation of Generator Output with Void Fraction

The change in the generator output with the fluid, gaseous, void volume fraction is shown in Fig. 32. The ordinate gives the power which is dissipated in the external resistance and is therefore proportional to the total generator output. The power increases as the void fraction is increased. This occurs even though the two-phase conductivity decreases more rapidly than does the increase in velocity due to the presence of voids; that is, in the range $0 < \alpha < 0.75$,

$$\sigma_{TP}\left(U_m^2/(1-\alpha)^2\right) < \sigma U_m^2.$$

The increase in power with increasing void fraction can be seen to be due to the variation of loading on the generator, $R_o/R_{i,TP}$, with void fraction (α). Since the generator power is given by

$$P_\alpha = 4abL\left(\frac{U_m}{1-\alpha}\right)^2 B_o^2 \sigma_{TP}\ \eta'\left[1 - \eta'\left(1 + \frac{2\ln 2}{c\,\pi}\right)\right],$$

and since

$$\sigma_{TP} = \sigma e^{-3.8\alpha},$$

and

$$\eta' = \left(\frac{R_{i,TP}}{R_o} + 1 + \frac{2 \ln 2}{c \pi} \right)^{-1} = \left(\frac{\sigma}{\sigma_{TP}} \frac{R_i}{R_o} + 1 + \frac{2 \ln 2}{c \pi} \right)^{-1}$$

$$= \left(\frac{e^{3.8\alpha}}{R_o/R_i} + 1 + \frac{2 \ln 2}{c \pi} \right)^{-1},$$

then the generator power becomes

$$P_\alpha = \frac{K_1(R_i/R_o)}{(1-\alpha)^2 \{(R_i/R_o) e^{3.8\alpha} + 1 + [(2 \ln 2)/c \pi]\}^2}, \qquad (79)$$

where

$$K_1 = 4abLU_m^2 B_o^2 \sigma.$$

For $\alpha = 0$,

$$P_{\alpha=0} = \frac{K_1(R_i/R_o)}{R_i/R_o + 1 + (2 \ln 2)/c \pi}. \qquad (80)$$

The power output of the generator is quite sensitive to the void volume fraction and the initial generator loading R_o/R_i.
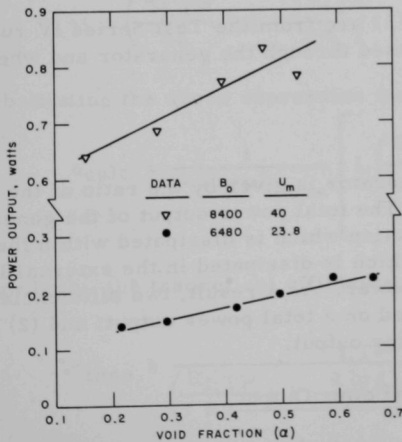
Fig. 32

Usable Power Output versus Void Fraction in Test Series IV

DATA	B_o	U_m
▽	8400	40
●	6480	23.8

A clearer picture of the variation of power with void fraction and R_o/R_i can be obtained from Fig. 33 where the normalized power ratio $(P_\alpha/P_{\alpha=0})$ is plotted as a function of the void fraction. These curves were

computed from Eqs. (79) and (80) and the empirical σ_{TP}-α relationship given by Eq. (68). A family of curves representing varying conditions of external-to-internal generator loadings is obtained. For initial loadings of $R_o/R_i < 4$, the power output drops as gaseous voids are introduced into the generator at a fixed liquid flow rate. The smaller the value of R_o/R_i, the larger the drop in power. For loadings of $R_o/R_i > 4$, the power output increases with increasing void fraction. At $R_o/R_i > 10$, the increases in power over the non-voided condition are very large and increase sharply with increasing void content.
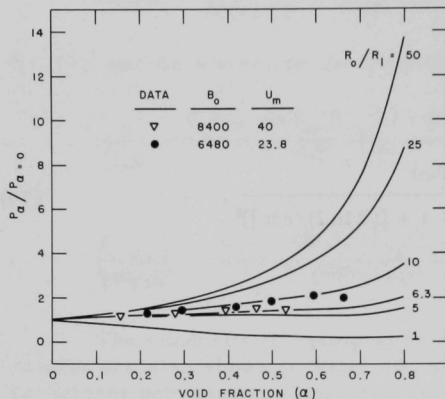
Fig. 33. Normalized Power versus Void Fraction

All curves would be expected to reach a maximum and then drop off suddenly as α approaches unity, since the conductivity-void fraction relationship would be expected to change in this region. The conductivity of the two-phase mixtures should drop off more rapidly in the void region $\alpha > 0.90$ than indicated by Eq. (68).

The data points shown on Fig. 33 are from the Test Series IV runs where the two-phase mixture was passed through the generator and where $R_o/R_i = 5.6$.

F. Generator Efficiency

The efficiency of the MHD generator is given by the ratio of the power output to the flow-work input. The total power output of the generator consists of two segments: (1) the fraction which is dissipated within the generator walls; and (2) the portion which is dissipated in the external loads, R_{sh} and R_{ss}, and represents usable power. As a result, two efficiencies may be defined: (1) an efficiency based on a total power output; and (2) an efficiency based on the usable generator output.

1. Efficiency Based on Total Power Output

For the nonideal generator studied in this investigation, the theoretical efficiency is

$$\epsilon_{theo} = \frac{P_\alpha}{P_p} = \eta' \left[1 - \eta' \left(1 + \frac{2 \ln 2}{c \pi} \right) \right] \bigg/ (1 - \eta'), \qquad (81)$$

where

$$\eta' = \left(\frac{R_{i,TP}}{R_o} + 1 + \frac{2\ln 2}{c\pi} \right)^{-1}.$$

The actual efficiency of the generator could not be determined directly since the portion of the generated power that was dissipated in the generator walls could not be measured. However, the pressure drop across the generator associated with the generated power was measured. Therefore, the calculated efficiency is given by

$$\epsilon_{calc} = \frac{P_\alpha}{P_p} = \frac{4abL\,\sigma_{TP} \left(\dfrac{U_m}{1-\alpha} \right)^2 B_o^2\,\eta' \left[1 - \eta' \left(1 + \dfrac{2\ln 2}{c\pi} \right) \right]}{(4ab) \left(\dfrac{U_m}{1-\alpha} \right) (-\Delta p_{TP})_{meas}}$$

$$= \frac{L\,\sigma_{TP}\,\dfrac{U_m}{1-\alpha}\,B_o^2\,\eta' \left[1 - \eta' \left(1 + \dfrac{2\ln 2}{c\pi} \right) \right]}{(-\Delta p_{TP})_{meas}}, \tag{82}$$

where $(-\Delta p_{TP})_{meas}$ is the measured pressure drop across the generator, and

$$\eta' = \left(\frac{R_{i,TP}}{R_o} + 1 + \frac{2\ln 2}{c\pi} \right)^{-1} = \left(\frac{\sigma}{\sigma_{TP}} \frac{R_i}{R_o} + 1 + \frac{2\ln 2}{c\pi} \right)^{-1}.$$

Substituting the above expression for η' into Eq. (82) and simplifying produce

$$\epsilon_{calc} = \frac{1}{(-\Delta p_{TP})_{meas}} \left[L \left(\frac{U_m}{1-\alpha} \right) B_o^2 \frac{(R_i/R_o)\sigma}{\left(1 + \dfrac{2\ln 2}{c\pi} + \dfrac{R_i}{R_o} \dfrac{\sigma}{\sigma_{TP}} \right)^2} \right]. \tag{83}$$

Similarly, the theoretical efficiency can be expressed as

$$\epsilon_{theo} = \frac{R_{i,TP}/R_o}{\left(\dfrac{R_{i,TP}}{R_o} + 1 + \dfrac{2\ln 2}{c\pi} \right) \left(\dfrac{R_{i,TP}}{R_o} + \dfrac{2\ln 2}{c\pi} \right)}. \tag{84}$$

It can be seen from the efficiency equations that ϵ_{theo} is a function of flow channel geometry, aspect ratio c, and the ratio $R_{i,TP}/R_o$. In the present experiments, c is a fixed value and the only values of R_i/R_o for

the single-phase runs are 0.156 for Test Series I, and 0.180 for Test Series II. However, for Test Series III and IV in which two phases were present, $R_{i,TP}$ is a function of σ_{TP} which, in turn, is a function of the void fraction (α). Therefore, sufficient data points are available to compare the theoretical efficiency with the calculated efficiency. As shown on Fig. 34, a substantial amount of scatter exists since the calculated efficiency is based on the measured Δp. This also suggests that the pressure drop measurements were not consistent. However, the maximum deviation is $<20\%$. This attests to the accuracy of the σ_{TP}-α relationship that was developed from the data, since the theoretical pressure drop is directly proportional to σ_{TP} [see Eq. (42)].
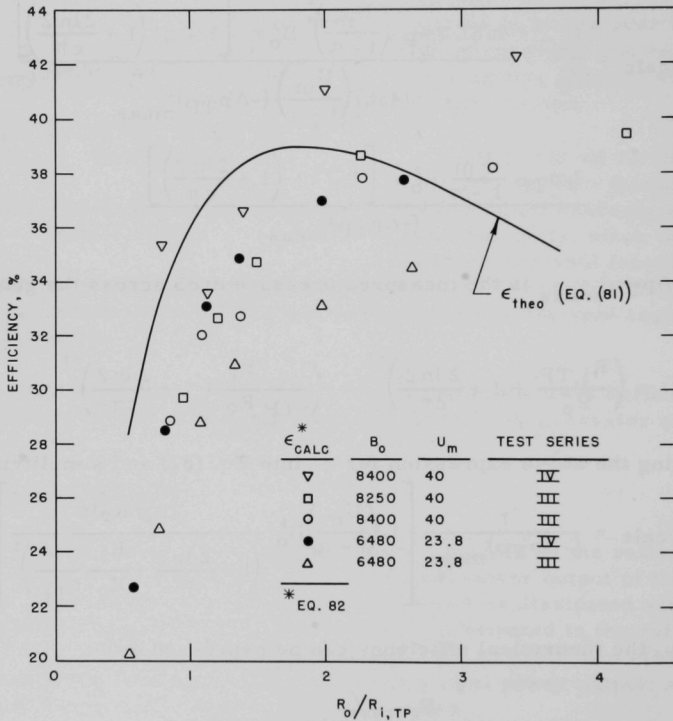
Fig. 34. Calculated versus Theoretical Generator
Efficiency Based upon Total Power Output

2. Efficiency Based on Usable Generator Output

The usable power output from the MHD generator is $V_2 I_2$ (see Fig. 4), or $V_2^2/(R_{sh} + R_{ss})$. Therefore, the experimental efficiency of the generator is

$$\epsilon_{exp} = \frac{(V_{2,TP})^2/(R_{sh}+R_{ss})}{4ab\left(\dfrac{U_m}{1-\alpha}\right)(-\Delta p_{TP})_{meas}} \quad (85)$$

Since $V_{2,TP}$, U_m, α, and Δp_{TP} are measurable quantities, ϵ_{exp} can be calculated directly from the data. However, $V_{2,TP}$ and $-\Delta p_{TP}$ can also be obtained theoretically; hence, ϵ_{theo} becomes

$$\epsilon_{theo} = \left[\frac{1}{R_{sh}+R_{ss}}\right]\left[\frac{\dfrac{R_{sh}+R_{ss}}{R_{BB}+R_{sh}+R_{ss}}\left(2a\,\eta'\dfrac{U_m}{1-\alpha}B_o\right)}{1+\dfrac{2R_c}{R_w}+\dfrac{R_c}{R_{BB}+R_{sh}+R_{ss}}}\right]^2 \Bigg/$$

$$4baL(1-\eta')\,\sigma_{TP}\left(\frac{U_m}{1-\alpha}\right)^2 B_o^2. \quad (86)$$

Substituting the known values of R_{sh}, R_{ss}, and R_{BB} into Eq. (86) and simplifying produce:

$$\epsilon_{theo} = \frac{2a(0.932)^2}{2bL\,\sigma_{TP}(1306.1\times10^{-6})\left(\dfrac{R_{i,TP}}{R_o}+0.239\right)\left(\dfrac{R_{i,TP}}{R_o}+1.239\right)}. \quad (87)$$

Figure 35 compares the experimental and theoretical efficiencies; the agreement is excellent. The actual efficiencies are extremely low because the walls of the generator are conducting and because their resistance is quite low in comparison to the external loads. As a result, ~90% of the generated power short-circuits through, and is dissipated in, the generator walls.
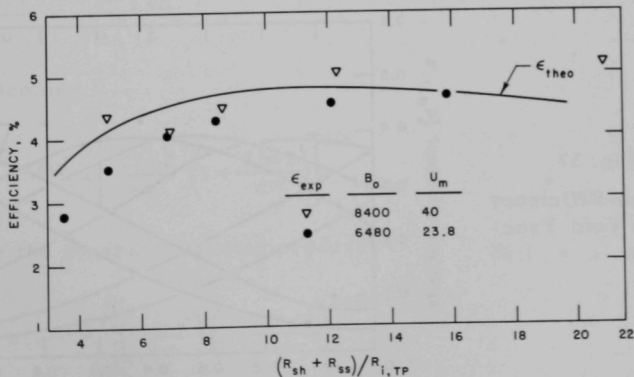
Fig. 35. Experimental versus Theoretical Generator Efficiency
Based upon Usable Power Output in Test Series IV

An overall view of the variation of the generator efficiency with void fraction is shown in Figs. 36 and 37. Figure 36 is a plot of the calculated normalized efficiency $\epsilon_\alpha / \epsilon_{\alpha=0}$ versus the void fraction. The efficiency ratio was calculated in the same manner as the power ratio. The results are a family of curves for various initial values of external generator loadings. In general, the trends are similar to those shown in Fig. 33 for the normalized generator power output. The data points are from Test Series IV.
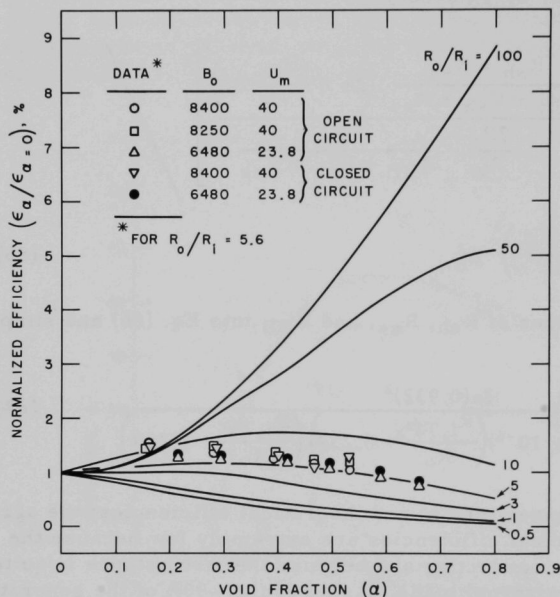
Fig. 36

Normalized Efficiency versus Void Fraction

Fig. 37

Absolute Efficiency versus Void Fraction for c = 1.85
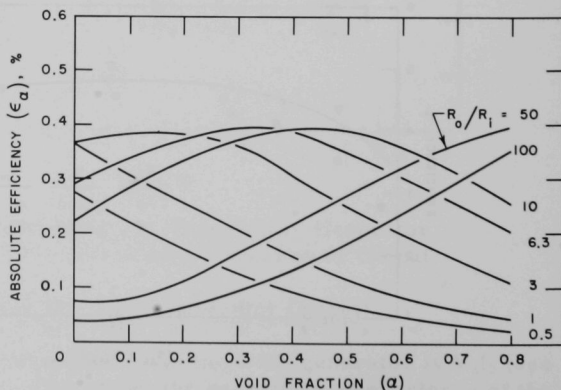
For values of $R_o/R_i < 3$, the normalized efficiency is less than unity, and continues to decrease with increasing void fraction. For values of $3 < R_o/R_i < 10$, the normalized efficiency rises above unity, reaches a maximum, and then decreases to values below unity as the void content increases. For $R_o/R_i > 10$, the efficiency ratio increases with increasing void content. Figure 36 indicates that there are large areas in which the generator efficiency does not degenerate due to the presence of voids. In fact, the performance characteristics of the generator are enhanced.

Figure 37 shows the absolute magnitude of the generator efficiency as a function of the void fraction and initial generator loading. The trends are similar to those of the normalized efficiency shown in Fig. 36. The maximum efficiency is a function of the generator loading R_o/R_i and the void fraction α. The maximum value of the efficiency and its dependence upon the void fraction and generator loading are obtained by differentiating the efficiency equation, Eq. (81), with respect to the generator load, $R_{i,TP}/R_o$. That is,

$$\frac{d\epsilon}{d(R_{i,TP}/R_o)} = d\left(\frac{\eta' \{1 - \eta' [1 + (2\ln 2)/c\pi]\}}{1 - \eta'} \right) \Bigg/ d(R_{i,TP}/R_o) = 0.$$

(88)

From Eq. (88) it can be shown that, for the condition that the efficiency be maximum,

$$\frac{R_{i,TP}}{R_o} = \left[\frac{2\ln 2}{c\pi} \left(1 + \frac{2\ln 2}{c\pi} \right) \right]^{1/2}.$$

(89)

Since

$$\frac{R_{i,TP}}{R_o} = \frac{R_i}{R_o} e^{3.8\alpha},$$

Eq. (89) becomes

$$\frac{R_i}{R_o} e^{3.8\alpha} = \left[\frac{2\ln 2}{c\pi} \left(1 + \frac{2\ln 2}{c\pi} \right) \right]^{1/2}.$$

(90)

Solving for the generator loading produces

$$\frac{R_o}{R_i} = e^{3.8\alpha} \Bigg/ \left[\left(\frac{2\ln 2}{c\pi} \right) \left(1 + \frac{2\ln 2}{c\pi} \right) \right]^{1/2}.$$

(91)

Equation (91) establishes the initial generator loading to achieve maximum efficiency under voided operating conditions for a specified generator geometry. There is virtually a limitless number of combinations of generator loading and fluid void fraction that will yield the maximum generator efficiency, whereas the nonvoided generator ($\alpha = 0$) requires a unique loading to achieve the maximum efficiency. Regardless of the relationship used for predicting the two-phase conductivity, the behavior pattern shown in Fig. 37 will hold. The introduction of voids into an MHD generator does not automatically reduce the generator efficiency.

The maximum efficiency that can be attained in an MHD generator is determined by the magnitude of the end losses occurring in the generator and is independent of the generator loading and fluid conductivity. This can be seen by substituting Eq. (89) into Eq. (81). The efficiency becomes

$$\epsilon_{max} = \left\{ \left(1 + \frac{4 \ln 2}{c \pi}\right) + 2 \left[\left(\frac{2 \ln 2}{c \pi}\right) \left(1 + \frac{2 \ln 2}{c \pi}\right)\right]^{1/2} \right\}^{-1}. \qquad (92)$$

As is evident from Eq. (92), the upper bound on the efficiency is dependent only upon the generator geometry and, more specifically, on the ratio of the generator length to width (c). The relationship given by Eq. (92) is based on the end-loss factor given by Sutton[13] for the abrupt termination of the magnetic field at the electrode ends. As mentioned previously, this factor was judged to be quite accurate.
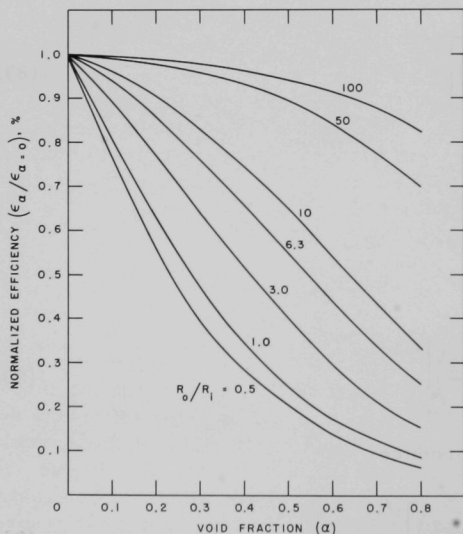
The variance in performance between the ideal generator with no end losses and the non-ideal generator studied in this investigation is illustrated by comparing Figs. 36 and 37 with Figs. 38 and 39. In Figs. 38 and 39, the normalized and absolute generator efficiencies for an ideal generator are plotted against the void volume fraction and generator loading.

From Eq. (81), the absolute efficiency for an ideal generator, when the end-loss correction factor ($2 \ln 2/c\pi$) is set equal to zero, is given by

Fig. 38. Normalized Efficiency versus Void Fraction for an Ideal MHD Generator
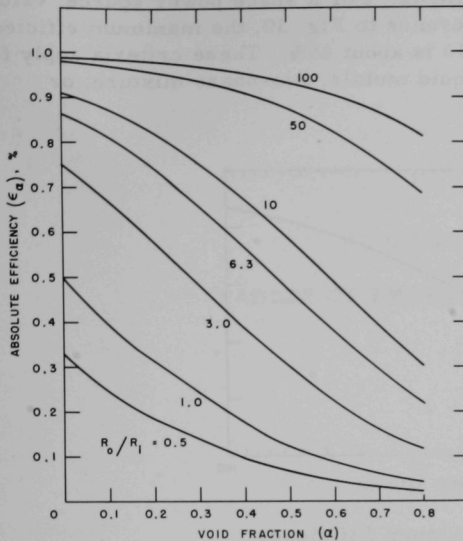
$$\epsilon = [1 + (R_i/R_o)e^{3.8\alpha}]^{-1}.$$

Fig. 39

Absolute Efficiency versus
Void Fraction for an Ideal
MHD Generator

The normalized ideal generator efficiency becomes

$$\frac{\epsilon_\alpha}{\epsilon_{\alpha=0}} = \frac{1 + (R_i/R_o)}{1 + (R_i/R_o)e^{3.8\alpha}}$$

The trends for the ideal generator are different from those shown in Figs. 36 and 37, for the nonideal generator studied. Both the normalized efficiency and the absolute efficiency decrease with increasing void fraction for all generator loadings. However, as the generator loading is increased, both efficiencies approach unity as the limiting case. It should be remembered that the analyses presented are for the case

$$\frac{Ha}{Ha - \tanh Ha} = 1.$$

This condition is approximated when $Ha > 100$.

The ideal generator with no end losses is not readily attained in actual practice. To illustrate the dependency of generator efficiency on the end losses, a graph of Eq. (92) is shown in Fig. 40. The efficiency decreases rapidly as the channel aspect ratio (c) is reduced. To achieve generator efficiencies of ~90%, the ratio c would have to be 200 or greater. The condition that the end-loss factor be essentially zero (the ideal generator case) is met when $c \gtrsim 2200$. The value of c that is feasible from a practical viewpoint is not clear-cut. For a commercial system, an aspect

ratio of 10 or higher may be acceptable. For a space power source, values of 10 appear mandatory. With reference to Fig. 30, the maximum efficiency one could hope to attain with c = 10 is about 65%. These criteria apply for all fluids, whether single-phase liquid metals, two-phase mixture, or plasma.
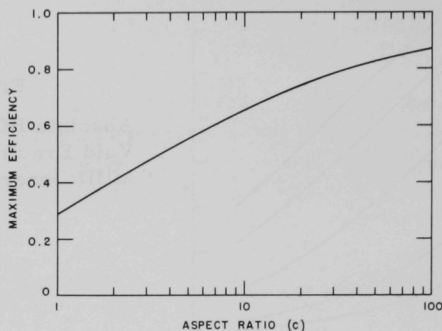
Fig. 40. Maximum Efficiency
versus Aspect Ratio

APPENDIX A

TABLES OF EXPERIMENTAL DATA

Table A-1

SUMMARY OF TEST SERIES I: NaK (OPEN CIRCUIT)

Run No.	B_O, Gauss	NaK Flow Rate, lb/min	$(-\Delta p)_{meas}$, psi	$-\Delta p_1$,* psi	V_1, mV	Remarks
74	4350	107.0	4.31	3.90	44.68	See Figs. 10
75	4350	93.8	3.63	3.32	38.2	and 15
76	4350	76.8	2.75	2.55	30.05	
77	4350	53.4	1.88	1.80	19.68	
78	4350	33.8	0.86	0.84	12.3	
79	4350	17.0	0.50	0.50	6.23	
80	6400	106.0	8.96	8.55	67.35	See Figs. 10
81	6400	94.8	7.84	7.52	59.22	and 14
82	6400	85.8	6.93	6.67	52.58	
83	6400	74.6	5.91	5.72	45.33	
84	6475	65.3	4.98	4.85	38.68	
85	6475	46.5	3.47	3.42	27.47	
86	6475	24.2	1.75	1.74	14.53	
87	7320	95.5	9.67	9.35	66.0	See Figs. 13
88	7320	82.6	8.05	7.81	55.48	and 17
89	7320	69.5	6.57	6.41	45.82	
90	7350	54.5	4.86	4.78	34.62	
91	7350	38.4	3.36	3.33	24.54	
92	7350	25.5	2.05	2.04	15.5	
93	7940	88.2	10.16	9.89	64.5	See Figs. 12
94	7940	78.8	8.8	8.59	56.3	and 16
95	7940	66.2	7.12	6.98	46.24	
96	7940	50.0	5.16	5.10	34.15	
97	7940	32.5	3.48	3.46	22.8	
98	7940	20.8	1.95	1.95	13.8	
99	8450	81.6	10.37	10.14	63.0	See Figs. 11
100	8450	69.5	8.54	8.38	52.19	and 15
101	8450	55.5	6.57	6.48	40.84	
102	8450	39.8	4.60	4.57	29.35	
103	8450	24.2	2.80	2.79	18.43	
104	8450	15.0	1.80	1.80	12.27	
105	8800	74.6	10.17	9.98	59.7	See Figs. 10
106	8800	64.2	8.50	8.37	50.37	and 14
107	8800	47.5	6.04	5.98	36.77	
108	8800	30.0	3.77	3.75	23.6	
109	8800	18.2	2.18	2.18	13.87	

*$-\Delta p_1 = (-\Delta p)_{meas}$ = pressure drop due to friction.

Table A-2

SUMMARY OF TEST SERIES II: NaK (CLOSED CIRCUIT)

Run No.	B_0, Gauss	NaK Flow Rate, lb/min	$(-\Delta p)_{meas}$, psi	$-\Delta p_2$,* psi	V_2, mV	I_2, Amp	Remarks
110	4350	142.3	6.93	6.18	57.45	43.8	See Figs. 18,
111	4350	134.5	6.15	5.48	52.25	40.0	22, and 27
112	4350	121.0	5.15	4.61	45.37	34.8	
113	4350	107.0	4.51	4.10	39.9	30.6	
114	4350	93.8	3.83	3.52	34.25	26.2	
115	4350	77.7	3.0	2.79	27.23	20.8	
116	4350	62.0	2.36	2.24	21.28	16.2	
117	4350	42.0	1.53	1.49	14.11	10.8	
118	4350	25.5	0.9	0.89	8.22	6.2	
119	6500	104.2	9.37	8.98	58.52	45.0	See Figs. 18,
120	6500	93.0	8.07	7.77	50.55	38.8	22, and 26
121	6500	80.8	6.84	6.61	43.04	33.0	
122	6500	65.2	5.45	5.32	34.4	26.4	
123	6500	47.6	3.75	3.69	24.29	18.6	
124	6500	32.5	2.47	2.45	16.16	12.4	
125	6500	18.3	1.39	1.39	9.13	6.8	
126	7350	91.0	9.92	9.63	56.45	43.2	See Figs. 21,
127	7350	78.8	8.44	8.22	48.19	36.8	25, and 29
128	7350	68.5	7.11	6.96	40.83	31.2	
129	7350	53.5	5.38	5.30	31.43	24.0	
130	7350	38.3	3.75	3.72	22.16	17.0	
131	7350	24.3	2.40	2.39	14.2	10.8	
132	7350	14.5	1.5	1.5	8.98	6.8	
133	8000	84.5	10.38	10.13	55.33	42.6	See Figs. 20,
134	8000	75.8	9.12	8.92	48.73	37.4	24, and 28
135	8000	64.3	7.52	7.39	40.57	31.0	
136	8000	50.0	5.62	5.56	30.51	23.4	
137	8000	35.0	3.86	3.84	21.22	16.2	
138	8000	22.0	2.38	2.38	13.35	10.4	
139	8500	77.8	10.53	10.32	53.5	41.0	See Figs. 19,
140	8500	67.5	9.0	8.86	45.84	35.4	23, and 27
141	8500	50.0	6.46	6.40	33.34	25.6	
142	8500	36.0	4.54	4.52	23.61	18.2	
143	8500	20.8	2.64	2.64	13.64	10.4	
144	8900	67.4	9.68	9.54	47.73	36.8	See Figs. 18,
145	8900	73.5	10.69	10.51	52.32	40.2	22, and 26
146	8900	52.2	7.14	7.07	35.43	27.4	
147	8900	37.2	5.02	4.99	25.39	19.8	
148	8900	25.5	3.33	3.32	17.23	13.2	
149	8900	14.6	1.84	1.84	9.27	7.0	

*$-\Delta p_2 = (-\Delta p)_{meas}$ = pressure drop due to friction.

Table A-3

SUMMARY OF TEST SERIES III: NaK-N_2 (OPEN CIRCUIT)

Run No.	B_O, Gauss	NaK Flow Rate, lb/min	N_2 Flow Rate, lb/min	Void Fraction	$-\Delta p_{1,TP}$, psi	$V_{1,TP}$, mV	Remarks
258	6480	23.8	0	0	1.63	13.4	See Fig. A-1.
259	6480	23.8	0.027	0.117	1.57	15.5	Void fraction
260	6480	23.8	0.048	0.188	1.57	16.0	measured by
261	6480	23.8	0.111	0.31	1.56	17.0	γ-ray tech-
262	6480	23.8	0.175	0.395	1.63	17.8	nique at outlet
263	6480	23.8	0.285	0.523	1.68	18.8	of generator
264	6480	23.8	0.377	0.603	1.73	19.0	flow channel.
266	6480	23.8	0	0	1.60	13.4	See Fig. A-1.
267	6480	23.8	0.027	0.3	1.57	15.5	Void fraction
268	6480	23.8	0.048	0.42	1.57	16.0	measured at
269	6480	23.8	0.111	0.545	1.56	17.0	inlet of gen-
270	6480	23.8	0.175	0.623	1.63	18.0	erator flow
271	6480	23.8	0.285	0.67	1.68	18.8	channel.
272	6480	23.8	0.377	0.73	1.73	19.0	
300	8400	40.0	0	0	4.47	29.2	See Fig. A-2.
301	8400	40.0	0.041	0.212	4.08	32.8	Void fraction
302	8400	40.0	0.109	0.35	4.11	35.5	measured at
303	8400	40.0	0.22	0.465	4.10	36.0	inlet of gen-
304	8400	40.0	0.315	0.537	3.92	37.0	erator flow channel.
305	8270	40.0	0.390	0.57	3.99	37.7	See Fig. A-2.
316	8250	40.0	0.041	0.097	4.20	33.8	Void fraction
317	8250	40.0	0.109	0.21	3.87	34.8	measured at
318	8250	40.0	0.22	0.327	3.98	36.5	outlet of gen-
319	8250	40.0	0.315	0.41	4.05	38.0	erator flow channel.
320	8170	40.0	0.392	0.502	4.12	39.0	

Table A-4

SUMMARY OF TEST SERIES IV: NaK-N_2 (CLOSED CIRCUIT)

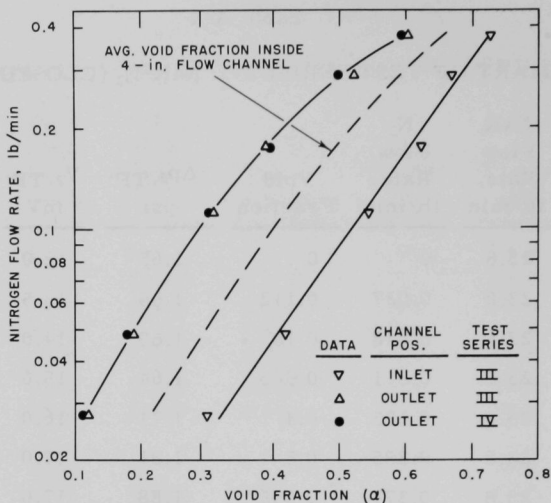| Run No.	B_o, Gauss	NaK Flow Rate, lb/min	N_2 Flow Rate, lb/min	Void Fraction	$-\Delta p_{2,TP}$, psi	$V_{2,TP}$, mV	Remarks
273	6480	23.8	0	0	1.65	12.0	See Fig. A-1.
274	6480	23.8	0.027	0.112	1.65	13.5	Void fraction measured at
275	6480	23.8	0.048	0.18	1.63	14.0	outlet of generator flow
276	6480	23.8	0.111	0.305	1.64	15.0	channel.
277	6480	23.8	0.175	0.4	1.71	16.0	
278	6480	23.8	0.285	0.5	1.81	17.0	
279	6480	23.8	0.377	0.595	1.88	17.0	
293	8400	40.0	0	0	4.79	26.4	See Fig. A-2.
294	8400	40.0	0.041	0.095	4.38	29.0	Void fraction measured at
295	8400	40.0	0.109	0.205	4.10	30.0	outlet of generator flow
296	8400	40.0	0.22	0.315	4.35	31.8	channel.
297	8400	40.0	0.315	0.393	4.52	33.0	
298	8270	40.0	0.392	0.485	3.54	32.0	

60

Fig. A-1. Average Void Fraction in the MHD
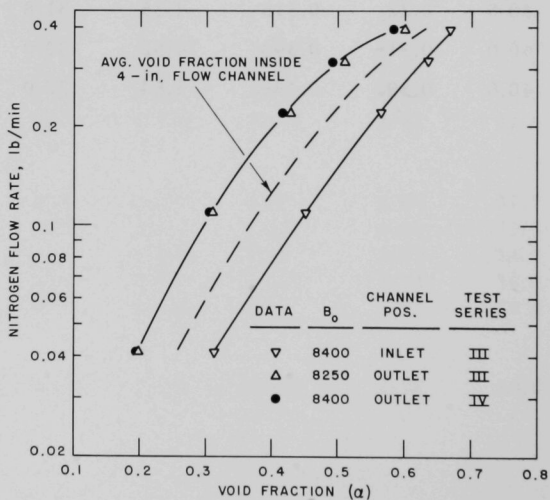Generator for U_m = 23.8 lb/min;
B_0 = 6480 Gauss

Fig. A-2. Average Void Fraction in the MHD
Generator for U_m = 40 lb/min;
B_0 = 8400 and 8250 Gauss

APPENDIX B

TABLES OF CALCULATED DATA

Table B-1

SUMMARY OF TEST SERIES I: NaK (OPEN CIRCUIT)

B_0, Gauss	V_1, mV	V_1', mV	$-\Delta p_1$, psi	$-\Delta p_1'$, psi
4350	$0.402U_m$	$0.485U_m$	$0.044U_m$	$0.021U_m$
6400	$0.591U_m$	$0.713U_m$	$0.095U_m$	$0.045U_m$
7320	$0.676U_m$	$0.816U_m$	$0.125U_m$	$0.060U_m$
7940	$0.733U_m$	$0.885U_m$	$0.147U_m$	$0.070U_m$
8450	$0.780U_m$	$0.942U_m$	$0.166U_m$	$0.079U_m$
8800	$0.813U_m$	$0.980U_m$	$0.180U_m$	$0.086U_m$

Remarks:

   (1) For V_1 and V_1', see Figs. 10 to 13.
   (2) For $-\Delta p_1$ and $-\Delta p_1'$, see Figs. 14 to 17.
   (3) U_m is NaK flow rate in lb/min.
   (4) V_1 and $-\Delta p_1$ are the values with end-loss correction.
   (5) V_1' and $-\Delta p_1'$ are the values without end-loss correction.

Table B-2

SUMMARY OF TEST SERIES II: NaK (CLOSED CIRCUIT)

B_0, Gauss	V_2, mV	V_2', mV	I_2, Amp	I_2', Amp	$-\Delta p_2$, psi	$-\Delta p_2'$, psi
4350	$0.368U_m$	$0.443U_m$	$0.282U_m$	$0.339U_m$	$0.046U_m$	$0.024U_m$
6500	$0.550U_m$	$0.661U_m$	$0.421U_m$	$0.506U_m$	$0.103U_m$	$0.053U_m$
7350	$0.622U_m$	$0.748U_m$	$0.476U_m$	$0.573U_m$	$0.131U_m$	$0.068U_m$
8000	$0.677U_m$	$0.814U_m$	$0.518U_m$	$0.623U_m$	$0.155U_m$	$0.080U_m$
8500	$0.719U_m$	$0.865U_m$	$0.551U_m$	$0.662U_m$	$0.175U_m$	$0.091U_m$
8900	$0.753U_m$	$0.906U_m$	$0.577U_m$	$0.693U_m$	$0.192U_m$	$0.099U_m$

Remarks:

   (1) For V_2 and V_2', see Figs. 18 to 21.
   (2) For I_2 and I_2', see Figs. 22 to 25.
   (3) For $-\Delta p_2$ and $-\Delta p_2'$, see Figs. 26 to 29.
   (4) V_2, I_2, and $-\Delta p_2$ are the values with end-loss correction.
   (5) V_2', I_2', and $-\Delta p_2'$ are the values without end-loss correction.

Table B-3

SUMMARY OF TEST SERIES III: NaK-N$_2$ (OPEN CIRCUIT)

B_o, Gauss	NaK Flow Rate, lb/min	$1 - \alpha_{avg}$	$(V_{1,TP})_{meas}$, mV	$\dfrac{\sigma}{\sigma_{TP}}$	$\left(\dfrac{\sigma}{\sigma_{TP}}\right)'$
6480	23.8	0.785	15.5	2.53	4.06
6480	23.8	0.705	16.0	3.35	4.88
6480	23.8	0.582	17.0	4.93	6.46
6480	23.8	0.505	18.0	6.07	7.60
6480	23.8	0.41	18.8	8.58	10.11
6480	23.8	0.34	19.0	11.78	13.31
8250	40	0.845	33.8	1.60	3.13
8250	40	0.72	34.8	2.94	4.47
8250	40	0.605	36.5	4.40	5.93
8250	40	0.535	38.0	5.47	7.00
8250	40	0.47	39.0	6.93	8.46
8400	40	0.845	32.8	2.07	3.60
8400	40	0.72	35.5	2.92	4.45
8400	40	0.605	36.0	4.80	6.33
8400	40	0.535	37.0	6.08	7.61
8400	40	0.47	37.7	7.72	9.25

Remarks:

(1) $\dfrac{\sigma}{\sigma_{TP}}$ are the values with end-loss correction. (See Fig. 30.)

(2) $\left(\dfrac{\sigma}{\sigma_{TP}}\right)'$ are the values without end-loss correction.
(See Fig. 31.)

(3) α_{avg} values are obtained from Figs. A-1 and A-2.

Table B-4

SUMMARY OF TEST SERIES IV: NaK-N$_2$ (CLOSED CIRCUIT)

α_{avg}	$1 - \alpha_{avg}$	$\dfrac{U_m}{1 - \alpha_{avg}}$	$\left(V_{2,TP}\right)_{meas}$, mV	$\dfrac{\sigma}{\sigma_{TP}}$	$\left(\dfrac{\sigma}{\sigma_{TP}}\right)'$
		U_m = 23.8 lb/min; B_O = 6480 Gauss			
0.215	0.785	30.32	13.5	2.83	4.16
0.295	0.705	33.76	14.0	3.55	4.87
0.418	0.582	40.89	15.0	4.91	6.23
0.495	0.505	47.13	16.0	5.86	7.18
0.590	0.410	58.05	17.0	7.89	9.21
0.660	0.340	70.00	17.0	10.93	12.25
		U_m = 40 lb/min; B_O = 8400 Gauss			
0.155	0.845	47.34	29.0	2.27	3.59
0.280	0.720	55.56	30.0	3.50	4.83
0.395	0.605	66.12	31.8	4.77	6.10
0.465	0.535	74.77	33.0	5.82	7.15
0.530	0.470	85.11	32.0	8.03	9.36

Remarks:

(1) $\dfrac{\sigma}{\sigma_{TP}}$ are the values with end-loss correction. (See Fig. 30.)

(2) $\left(\dfrac{\sigma}{\sigma_{TP}}\right)'$ are the values without end-loss correction.
(See Fig. 31.)

(3) α_{avg} values are obtained from Figs. A-1 and A-2.

Table B-5

GENERATOR EFFICIENCY BASED ON TOTAL POWER OUTPUT

B_o, Gauss	U_m, lb/min	Test Series	$(-\Delta P_{TP})_{meas}$, psi	$\left(\dfrac{\sigma}{\sigma_{TP}}\right)_{exp}$	$\dfrac{R_o}{R_{i,TP}}$	$1 - \alpha$	ϵ_{calc}, %
6480	23.8	III	1.57	2.53	2.63	0.785	34.6
6480	23.8	III	1.57	3.35	1.97	0.705	33.1
6480	23.8	III	1.56	4.93	1.33	0.582	30.9
6480	23.8	III	1.63	6.07	1.08	0.505	28.9
6480	23.8	III	1.68	8.58	0.76	0.41	24.9
6480	23.8	III	1.73	11.78	0.55	0.34	20.2
6480	23.8	IV	1.65	2.83	2.58	0.785	37.9
6480	23.8	IV	1.63	3.55	1.97	0.705	37.1
6480	23.8	IV	1.64	4.91	1.36	0.582	34.9
6480	23.8	IV	1.71	5.86	1.12	0.505	33.1
6480	23.8	IV	1.81	7.89	0.81	0.410	28.5
6480	23.8	IV	1.88	10.93	0.57	0.340	22.7
8400	40	IV	4.38	2.27	3.40	0.845	42.3
8400	40	IV	4.10	3.50	2.00	0.720	41.1
8400	40	IV	4.35	4.77	1.40	0.605	36.6
8400	40	IV	4.52	5.82	1.12	0.535	33.6
8400	40	IV	3.54	8.03	0.79	0.47	35.3
8400	40	III	4.08	2.07	3.22	0.845	38.2
8400	40	III	4.11	2.92	2.27	0.72	37.9
8400	40	III	4.10	4.80	1.37	0.605	32.7
8400	40	III	3.92	6.08	1.08	0.535	32.0
8400	40	III	3.99	7.72	0.84	0.47	28.8
8250	40	III	4.20	1.60	4.21	0.845	39.5
8250	40	III	3.87	2.94	2.25	0.72	38.6
8250	40	III	3.98	4.40	1.49	0.605	34.7
8250	40	III	4.05	5.47	1.20	0.535	32.7
8250	40	III	4.12	6.93	0.94	0.47	29.7

Table B-6

GENERATOR EFFICIENCY BASED ON USABLE POWER OUTPUT

B_o, Gauss	U_m, lb/min	Test Series	$-\Delta p_{TP\,meas}$, psi	$1 - \alpha$	$V_{2,TP}$, mV	$\left(\dfrac{\sigma}{\sigma_{TP}}\right)_{exp}$	$\dfrac{R_{sh} + R_{ss}}{R_{i,TP}}$	ϵ_{exp}, %
6480	23.8	IV	1.65	0.785	13.5	2.83	15.82	4.7
6480	23.8	IV	1.63	0.705	14.0	3.55	12.09	4.6
6480	23.8	IV	1.64	0.582	15.0	4.91	8.34	4.3
6480	23.8	IV	1.71	0.505	16.0	5.86	6.86	4.1
6480	23.8	IV	1.81	0.410	17.0	7.89	4.97	3.5
6480	23.8	IV	1.88	0.340	17.0	10.93	3.52	2.8
8400	40	IV	4.38	0.845	29.0	2.27	20.88	5.2
8400	40	IV	4.10	0.720	30.0	3.50	12.27	5.0
8400	40	IV	4.35	0.605	31.8	4.77	8.60	4.5
8400	40	IV	4.52	0.535	33.0	5.82	6.91	4.1
8400	40	IV	3.54	0.470	32.0	8.02	4.88	4.3

APPENDIX C
UNIT CONVERSION FACTORS

$$U_m \left(\frac{cm}{sec}\right) = \left(\frac{lb}{min}\right) \frac{1}{60} \left(\frac{min}{sec}\right) \frac{1}{54.3} \left(\frac{ft^3}{lb}\right) \frac{1}{0.575} \left(\frac{1}{in.^2}\right) 144 \left(\frac{in.^2}{ft^2}\right) 30.48 \left(\frac{cm}{ft}\right)$$

$$= 2.34289 U_m \ (lb/min).$$

$$B_o \left(Volt\text{-}sec/cm^2\right) = 10^{-8} B_o \ (Gauss).$$

$$V \ (mV) = \eta(2a)U_m B_o$$

$$= 2.16 \ (in.) \ 2.54 \left(\frac{cm}{in.}\right) 2.34289 \left(\frac{cm}{sec}\right) 10^{-8} \left(\frac{Volt\text{-}sec}{cm^2}\right) 1000 \left(\frac{mV}{Volt}\right)$$

$$= \left(12877.8 \times 10^{-8}\right) \eta U_m \ (lb/min) \ B_o \ (Gauss).$$

$$-\Delta p \ (psi) = (1 - \eta)L U_m \sigma B_o^2$$

$$= 4 \ (in.) \ 2.34289 \left(\frac{cm}{sec}\right) \frac{10^6}{42} \left(\frac{1}{ohm\text{-}cm}\right) 10^{-16} \left(\frac{Volt^2\text{-}sec^2}{cm^4}\right)$$

$$\times 1 \left(\frac{amp}{Volt/ohm}\right) 0.7376 \left(\frac{ft\text{-}lb_f}{Volt\text{-}amp\text{-}sec}\right) 12 \left(\frac{in.}{ft}\right) (2.54)^4 \left(\frac{cm^4}{in.^4}\right)$$

$$= (82.2 \times 10^{-10})(1 - \eta)U_m \ (lb/min) \ B_o^2 \ (Gauss^2).$$

REFERENCES

1. B. A. Spence (comp.), Magnetohydrodynamic Power Generation, A Bibliography, Avco-Everett Research Laboratory, AMP-110 (June 1963).

2. W. D. Jackson, Review of MHD Power Generator, AMU-ANL Conference on Direct Energy Conversion, November 4-5, 1963, ANL-6802 (December 1963), pp. 101-109.

3. D. H. Elliott, Two-Fluid Magnetohydrodynamic Cycle for Nuclear-Electric Power Conversion, ARS Journal, 32, No. 6 (1962), pp. 924-928.

4. G. A. Brown et al., MHD Power Generation with Liquid Metals, Proc., 5th Symposium on Engineering Aspects of MHD, Mass. Inst. of Tech. (April 1964).

5. J. P. Penhune, Energy Conversion in Laminar MHD Channel Flow, ASD-TR-61-294 (August 1961).

6. G. W. Sutton, The Theory of Magnetohydrodynamic Power Generators, G. E. Space Science Lab., R62SD990 (December 1962).

7. A. Sherman, Exact Solutions for Magnetohydrodynamic Channel Flows, G. E. Space Science Lab., R62SD991 (December 1962).

8. J. Hartmann, Hg-dynamics, Danske Videns. Selskab, Math-fys. Medd. 15, No. 6 (1937).

9. J. A. Shercliff, Steady Motion of Conducting Fluids in Pipes Under Transverse Magnetic Fields, Proc. Cambridge Phil. Soc., 49 (1953), pp. 136-144.

10. Ya. S. Uflyand, Flow Stability of a Conducting Fluid in a Rectangular Channel in a Transverse Magnetic Field, Soviet Phys.-Tech. Phys., 5, No. 10 (1961), pp. 1191-1193.

11. W. E. Williams, Magnetohydrodynamic Flow in a Rectangular Tube at High Hartmann Number, J. Fluid Mech., 16 (1963), pp. 262-268.

12. A. G. Ryabinin and A. I. Khozhainov, Steady-State Laminar Flow of an Electrically Conducting Fluid in a Rectangular Tube Under the Action of Ponderomotive Forces, Soviet Phys.-Tech. Phys., 7, No. 1 (1962), pp. 9-13.

13. G. W. Sutton et al., *Electrical and Pressure Losses in a Magnetohydrodynamic Channel Due to End Current Loops*, Trans. AIEE, Part I: Communications and Electronics, Issue No. 58 (1961), pp. 687-694.

14. M. Petrick and B. S. Swanson, *Radiation Attenuation Method of Measuring Density of a Two-Phase Fluid*, Rev. Sci. Instr., 29, No. 12 (1958), pp. 1079-1085.

15. H. H. Hooker and G. F. Popper, *A Gamma-Ray Attenuation Method for Void Fraction Determination in Experimental Boiling Heat Transfer Facilities*, ANL-5766 (1958).

16. J. C. Maxwell, *A Treatise on Electricity and Magnetism*, (3rd ed.; New York: Oxford University Press, 1904), Vol. 1.

ACKNOWLEDGMENTS